Temporal-specific roles of Fragile X mental retardation protein in the development of hindbrain auditory circuit

Xiaoyu Wang*[1,2], Ayelet Kohl*[3], Xiaoyan Yu[1], Diego A. R. Zorio[1], Avihu Klar[4], Dalit Sela-Donenfeld[#3] and Yuan Wang[#1]

* Equal first authors

Equal corresponding authors

1. Department of Biomedical Sciences, Program in Neuroscience, Florida State University College of Medicine, Tallahassee, FL 32306, USA

2. Division of Histology & Embryology, Key Laboratory for Regenerative Medicine of the Ministry of Education, Medical College, Jinan University, Guangzhou 510632, China

3. Koret School of Veterinary Medicine, Robert H. Smith Faculty of Agriculture, Food and Environment, The Hebrew University of Jerusalem, Rehovot 76100, Israel

4. Department of Medical Neurobiology IMRIC, Hebrew University Medical School, Jerusalem 91120, Israel

Corresponding Authors:

Yuan Wang, Ph.D.

1115 West Call Street, Florida State University, Tallahassee, FL 32306, USA

Phone: (850) 645-4934; Email: yuan.wang@med.fsu.edu

Dalit Sela-Donenfeld, Ph.D.

Koret School of Veterinary Medicine, The Hebrew University of Jerusalem, Rehovot 76100, Israel

Phone: (972) 89489533; Email: dalit.seladon@mail.huji.ac.il

Keywords: Crispr-Cas9; auditory circuit; Fragile X syndrome; autism spectrum disorder; RNA-binding proteins; axon development; axon fasciculation; axon targeting

Summary Statement

Deficiency of an RNA-binding protein, FMRP, negatively affects how auditory axons travel through the developing brainstem and establish proper synaptic connectivity in a timely manner.

Abstract

Fragile X mental retardation protein (FMRP) is an RNA-binding protein abundant in the nervous system. Functional loss of FMRP leads to sensory dysfunction and severe intellectual disabilities. In the auditory system, FMRP deficiency alters neuronal function and synaptic connectivity and results in perturbed processing of sound information. Nevertheless, roles of FMRP in embryonic development of the auditory hindbrain have not been identified. Here, we developed high-specificity approaches to genetically track and manipulate throughout development the Atho1^{+} neuronal cell type, which is highly conserved in vertebrates, in the cochlear nucleus of chicken embryos. We identified distinct FMRP-containing granules in the growing axons of Atho1^{+} neurons and post-migrating NM cells. FMRP downregulation via Crispr/Cas9 and shRNA techniques resulted in perturbed axonal pathfinding, delay in midline crossing, excess branching of neurites, and axonal targeting errors during the period of circuit development. Together, these results provide the first *in vivo* identification of FMRP localization and actions in developing axons of auditory neurons, and demonstrate the importance of investigating early embryonic alterations toward understanding the pathogenesis of neurodevelopmental disorders.

Introduction

The Fragile X mental retardation protein (FMRP; encoded by *Fmr1* gene) is an RNA-binding protein that regulates many aspects of gene expression and protein function (Bagni and Greenough, 2005; Bassell and Warren, 2008; Davis and Broadie, 2017). Functional loss of FMRP during development leads to Fragile X syndrome (FXS), an intellectual disability. Many FXS symptoms appear early in life, including increasing autism features and emerging sensory hyperarousal, anxiety, and hyperactivity (Hagerman et al., 2017). These clinical observations, along with FMRP expression throughout gestation (Abitbol et al., 1993; Hinds et al., 1993), implicate a role of FMRP in embryonic and early postnatal brains. While FMRP regulation of neurotransmission and synaptic plasticity plays important roles in relatively mature brains (Bagni and Zukin, 2019; Bear et al., 2004; Deng et al., 2013; Ferron et al., 2014), how FMRP regulates brain development during embryonic stages is largely unknown, except its involvement in cortical neurogenesis (Castrén, 2016).

Axon growth is a multi-event process of embryonic brain development, including axonogenesis, pathfinding, arborizing, and terminating on appropriate postsynaptic structures (reviewed in Chédotal and Richards, 2010; Comer et al., 2019; Stoeckli, 2018). Multiple lines of evidence support an involvement of FMRP in axonal development. In the *Drosophila* mushroom body, FMRP limits axonal growth and controls axonal pruning (Bodaleo and Gonzalez-Billault, 2016; Pan et al., 2004; Tessier and Broadie, 2008). In vertebrates, FMRP knockout results in excessive axonal branches in zebrafish motor neurons (Shamay-Ramot et al., 2015) and abnormal projection patterns in the mouse forebrain (Bureau et al., 2008; Scharkowski et al., 2018). FMRP also associates with RNAs that encode proteins involved in axonogenesis and synaptogenesis, including the microtubule-associated protein MAP1b (Bodaleo and Gonzalez-Billault, 2016), cell adhesion molecule Dscam (Jain and Welshhans, 2016), and the axon guidance cue netrin (Kang et al., 2019). However, the exact *in vivo* functions of FMRP in distinct axonal events are unclear.

Here, we investigated the roles of FMRP in axonal development of the auditory brainstem using the chick embryo as a model system. The avian nucleus magnocellularis (NM) and nucleus laminaris (NL) are structurally and functionally similar to the mammalian anteroventral cochlear nucleus (AVCN) and medial superior olive (MSO), respectively. NM/AVCN neurons receive temporally precise excitation from the auditory nerve, and in turn, send bilaterally segregated signals to NL/MSO. Bipolar neurons in NL and MSO are specialized to compute interaural time differences (ITDs), time disparities in the arrival of signals between the two ears, binaural cues critical for sound localization and segregation (Nothwang, 2016;

Overholt et al., 1992; Vonderschen and Wagner, 2014). Clinical studies have revealed a tight association between FMRP level and temporal performance and have found impaired temporal processing of visual and auditory information in FXS (Farzin et al., 2011; Hall et al., 2009; Kéri and Benedek, 2011; Kogan et al., 2004; Rais et al., 2018). Cellular studies have further identified structural and physiological abnormalities in AVCN and its target cell groups in FMRP knockout rodents (Brown et al., 2010; El-Hassar et al., 2019; Garcia-Pino et al., 2017; Lu, 2019; McCullagh et al., 2017; Rotschafer et al., 2015; Ruby et al., 2015; Strumbos et al., 2010; Wang et al., 2015a). Finally, the nucleotide and amino acid sequences of chicken FMRP are similar to human FMRP (Price et al., 1996; Wang et al., 2014). Thus, studying FMRP regulation of NM and NL neurons is functionally relevant toward understanding FXS. Additionally, the stereotyped pattern of axonal projection from NM to NL (**Fig. 1A**) provides a suitable model for mechanistic studies of axonal circuitry development (Allen-Sharpley and Cramer, 2012; Cramer et al., 2004; Seidl et al., 2014).

To track specific cell types and neural circuits in complex vertebrate brains, we developed several genetic tools to selectively label and manipulate NM precursors and neurons in developing chicken embryos. We have identified an early-onset FMRP localization in axons of NM precursors and neurons and discovered that FMRP is required for the orderly and timely development of multiple axon events. These findings provide novel insights into understanding the potential contribution of compromised embryonic brain development to FXS pathogenesis.

Results

Dissecting the axonal circuitry development of NM precursors and neurons

NM neurons project to NL bilaterally (**Fig. 1A**). NL neurons are bipolar, with dendrites extending dorsally and ventrally from the soma to form two segregated dendritic domains. Cell bodies of NL neurons align into a single sheet, resulting in separate dorsal and ventral dendritic neuropil laminas. Individual NM axons bifurcate and project to the dorsal neuropil of the ipsilateral NL and the ventral neuropil of the contralateral NL. This segregated innervation pattern forms the anatomical substrate for ITD computation.

To label NM precursors and neurons selectively, we combined genetic markers with spatially controlled plasmid expression (**Fig. 1B**). The progenitor dA1 cells located along the dorsal-most region of the caudal rhombic lip expresses a basic helix-loop-helix transcription factor atonal homolog 1 (Atoh1), which gives rise to excitatory neurons in the auditory brainstem and precerebellar nuclei (Farago et al., 2006; Fujiyama et al., 2009; Helms et al., 2000; Machold and Fishell, 2005; Maricich et al., 2009). To enhance the specific labeling of the auditory

neurons, we introduced a plasmid expressing the Atoh1-enhancer element upstream to Cre recombinase along with a Cre-dependent myristoylated-GFP (mGFP) reporter plasmid into rhombomeres 5-6 (r5-6), which contain NM and NL precursors, via *in ovo* electroporation (Avraham et al., 2009; Cramer et al., 2000; Helms et al., 2000; Kohl et al., 2012; Kohl et al., 2013; Lipovsek and Wingate, 2018; **Fig. S1**). The electroporated Cre-conditional mGFP sequence was integrated into the chick genome by applying the PiggyBac transposition method (Wang et al., 2009), allowing the prolonged expression of the reporter in the auditory neurons (Hadas et al., 2014; Lu et al., 2009). For more restricted NM labeling, we performed the electroporation at E2-2.5, before NL cells are born (Rubel et al., 1976). Following electroporation, $mGFP^+$ cell bodies exhibited a restricted distribution in anatomically defined NM on the transfected side when examined at later stages (**Fig. 1C**). Axons of $mGFP^+$ cells originated from NM and projected to NL bilaterally, exhibiting the characterized pattern of NM-NL projection (**Fig. 1C, D**). The transfection rate, as calculated as the percentage of $mGFP^+$ neurons among all neurons in NM, was 15.3% ± 10.3% (mean ± SD; n=8 embryos) ranging from 3.4% to 34.4% (**Fig. 1E**). No $mGFP^+$ cells were detected in the contralateral NM, NL, or surrounding brainstem regions. Thus, our genetic targeting of Atoh1-mGFP cells was predominantly the NM precursors, termed *Atoh1 precursors of NM* henceforth, that establish the NM-NL circuit.

Next, we examined the development of the NM circuit stage by stage. We previously demonstrated that Atoh1/dA1 cells across r2-7 give rise to two contralateral axon projections (Kohl et al., 2012; 2015). One projection originated from the caudal hindbrain and elongated in a dorsal funiculus (DF), while the other arose from the more anterior hindbrain and formed a lateral funiculus (LF; **Fig. 2A**). The *Atoh1 precursors of NM* located at r5-6 extended their axons within the DF bundle (**Fig. 2B**). On transverse sections at E4.5, $mGFP^+$ axons had crossed the midline and arrived at the location where the NM and NL will form (yellow arrows in **Fig. 2C**), as indicated by a midline crossing rate of 1.060 (n=7 embryos; **Fig. 2D-E**). On the ipsilateral side, $mGFP^+$ axons form a well-defined dorsal-to-ventral fascicule (white arrow in **Fig. 2C**), confirmed quantitatively by small axonal bundle width ratio (0.259, n=7 embryos; **Fig. 2D, F**). At E7, NL was separating from the NM with rostral-to-caudal progress (**Fig. S2**), consistent with a previous report (Hendricks et al., 2006). $mGFP^+$ axons arrived at the emerging NL on the contralateral side (white arrows). In contrast, the ipsilateral projection was not visible, which is consistent with the results of individual axonal reconstructions that showed no ipsilateral projection until E8 (Young and Rubel, 1986). At E9 and later, NM and NL were recognizable as individual nuclei. The ipsilateral projection of $mGFP^+$ cells to the dorsal neuropil of NL had formed, revealing the

characterized bilateral NM-NL projection (Fig.S2). To further confirm this connectivity at the synaptic level, E2 embryos were electroporated with SV2-GFP along with Atoh1 enhancers and the PiggyBac transposase (**Fig. 2G**), enabling the expression of GFP in presynaptic vesicles (Hadas et al., 2014; Kohl et al., 2012). SV2-GFP was detected in the dorsal NL ipsilaterally and ventral NL contralaterally at E9 (**Fig. 2H-I'**), confirming the segregated synaptic projection from Atoh1-NM neurons to NL.

Closer examination of NM axons within NL revealed a stage-dependent terminal maturation (**Fig. 3**). At E11-13, the incoming NM axons ended with a typical growth cone morphology with 1-5 filopodia (white arrows). These filopodia gradually disappeared and turned into bouton endings at E15 (yellow arrows). By post-hatch day 6 (P6), NM axons exhibited a mature terminal morphology (**Fig. S3, S4**). Immunostaining demonstrated a distribution of vesicular glutamate transporters (vGluT2) along the axon course of Atoh1 precursors of NM at E4.5 (**Fig. S5**). At E15, NM axonal terminals contain a presynaptic SNARE component, SNAP25 (**Fig. S6**), indicating functional synapses. The time frame of the terminal morphological change was similar between the ipsilateral and contralateral projections of NM neurons, which indicates that the maturation of presynaptic terminals from the two NM inputs to NL neurons is temporally synchronized, although the two inputs differ in their time of arrival at the target area.

Axonal localization of FMRP in NM precursors and neurons

FMRP is strongly expressed in hindbrain (**Fig. 4A**). It is not known whether FMRP is localized in NM axons, and if so, when this localization emerges during development. Here, we addressed this question by immunostaining endogenous FMRP and localizing ectopic FMRP. Embryos were electroporated with Atoh1-mGFP at E2. At E4-5 (n=5 embryos), $mGFP^+$ cells consistently showed somatic FMRP immunoreactivity (**Fig. 4B-B''**, **4C-C''**). Contralaterally, $mGFP^+$ axons terminated in a cell-free region where FMRP staining is generally low (yellow arrows in **Fig. 4B-B''**). Closer observation demonstrated distinct FMRP puncta in this region (**Fig. 4D'**). These puncta were 0.2 to 0.7 µm in diameter, with an average density of 4.3 puncta per 100 μm^2 (28 sections from 5 embryos). A subset of FMRP puncta overlapped with $mGFP^+$ axon processes (**Fig. 4D- E**), confirming FMRP localization in distal axons of NM precursors.

We next determined whether FMRP is localized in NM axons at late embryonic stages when they have formed synaptic connectivity with NL neurons. During this time window (E9 to E19), the neuropil regions of NL contain a mixture of NM axons, NL dendrites, and astrocyte processes. We developed a transposon-based vector system expressing chick FMRP (chFMRP) fused with mCherry (**Fig. 5A**) for constitutive expression (Schecterson et al., 2012). At E4, $mCherry^+$ puncta were identified in the fibrous area where contralateral axons of NM

precursors terminate (**Fig. S7**), consistent with the localization of endogenous FMRP puncta shown in Fig. 4. We co-electroporated E2 embryos with chFMRP-mCherry and Atoh1-mGFP (**Fig. 5B**) and harvested brainstem sections between E9 and E19 (n=13 embryos). A substantial number of NM cells expressed chFMRP-mCherry on the transfection side (**Fig. 5C**, left column). In addition, mCherry$^+$ NL neurons were seen on the same side in some cases. To avoid this confounding factor, further analyses were performed in the contralateral NL in which mCherry labeling was exclusively derived from transfected NM axons. Across all cases, mCherry$^+$ puncta were identified in the fiber region between NL and the ventral brainstem, which contains incoming NM axons, as well as within the ventral neuropil domain of NL (**Fig. 5C,** right column). This localization pattern indicates that the introduced chicken FMRP is localized in the distal portions of NM axons. This is further confirmed by the presence of mCherry$^+$ puncta in Atoh1-mGFP expressing axons (**Fig. 5D**). Next, we replaced chFMRP-mCherry with human FMRP (hFMRP)-EGFP in the plasmid (**Fig. 5A**) and identified a similar pattern of FMRP distribution (**Fig. 5E**). This result implicates that the sequence of FMRP underlying its axon localization in NM axons is conserved between birds and humans.

FMRP deficiency affects axonal growth pattern of NM precursors

In vitro studies implicate FMRP regulation in neurite outgrowth (Doers et al., 2014), axon elongation (Wang et al., 2015b), and branching (Zimmer et al., 2017). Together with our finding that *Atoh1 precursors of NM* contain FMRP in distal axons (Fig. 4), these studies raise the possibility that FMRP regulates axonal growth and pathfinding of NM precursors *in vivo*. We examined this possibility by determining the effects of downregulating FMRP on axon development of *Atoh1 precursors of NM*.

Crispr-mediated FMRP knockout. We first downregulated FMRP in Atoh1$^+$ neurons using the Crispr (clustered regularly interspaced short palindromic repeats)/Cas9 system (Cong et al., 2013; Hille and Charpentier, 2016). Two guide RNAs ($gRNA_3$ and $gRNA_4$) were designed to target exon 8 of FMRP coding sequence to cause a deletion of ~260 bp (**Fig. 6A; Table 1**). To verify this deletion, $gRNA_{3+4}$ plasmids, which contain Cas9 and GFP on the same pCAG-construct, were co-electroporated into the dorsal-most region of E2.5 embryos. Control embryos were electroporated with a control-gRNA construct ($gRNA_{control}$; Table 1). While both $gRNA_{control}$ and $gRNA_{3+4}$ electroporated embryos demonstrated a 459 bp fragment of the size of intact *Fmr1* sequence, $gRNA_{3+4}$ embryos also presented a lower-size band of 260 bp (**Fig. 6B**, red arrow), which reflects the deletion of ~200 bp in electroporated cells. Next, we confirmed that this deletion prevents FMRP synthesis. At E6.5 (n=7 embryos), the majority of GFP$^+$ cells (80%) were FMRP immunoreactive in embryos electroporated with $gRNA_{control}$ (**Fig. 6C-C''**, arrows). In

contrast, only 10% of GFP$^+$ cells expressed FMRP following gRNA$_{3+4}$ expression (**Fig. 6D-D''**, arrowheads; **Fig. 6E**). Finally, we confirmed that expression of gRNA$_{control}$ and gRNA$_{3+4}$ plasmids was confined to dA1 neurons, showing the overlapping expression of GFP with Lhx2/9 (**Fig. 6F-H**), a specific marker for dA1/Atoh1$^+$ interneurons (Bermingham et al., 2001; Gray, 2013; Kohl et al., 2012).

FMRP knockout induces axon growth defects. To examine whether FMRP knockout affects dA1 axonal projections, embryos were electroporated with RNA$_{control}$ or gRNA$_{3+4}$ CAG plasmids at E2.5 and harvested at E4.5 (n=7-10 embryos for each plasmid) and E6.5 (n=6-9 embryos for each plasmid). These time points encompass the period during which dA1 interneurons extend their axons along a well-defined dorsal-to-ventral fascicule, cross the midline, and project in a parallel ventral-to-dorsal trajectory until reaching the contralateral auditory nuclei anlage (Fig. 2C; Kohl et al., 2012). As expected, flat-mount views of E4.5 control embryos exhibited this typical trajectory of dA1 axons that cross the midline (**Fig. 7A-A'**, arrows), indicating unaffected axonal growth with gRNA$_{control}$ expression. Observations from transverse sections further demonstrated that these axons projected in a fasciculated lateral bundle in the ipsilateral route and projected to the contralateral side (**Fig. 7C-C'** arrows). Strikingly, many gRNA$_{3+4}^+$ expressing axons did not extend toward the floor plate and showed disorganized ipsilateral routes (**Fig. 7B-B'**, dashed arrows). Observations from transverse sections confirmed that axons projected ventrally in a broad mediolateral pattern rather than in a directional ventrolateral route as well as extended medially toward the ventricle (**Fig. 7D-E'**, arrowheads). Quantitative analyses (as illustrated in Fig. 2D) revealed that the width of the GFP$^+$ axonal bundle, measured in the circumferential axis, was significantly greater in gRNA$_{3+4}$ electroporated embryos than the control embryos (**Fig. 7H**; non-parametric p<0.001; Mann-Whitney test for this and all following comparisons). In addition, the angle of individual axons in relation to the mantle zone angle of the neural tube (Fig.2D) was significantly increased following FMRP knockout (p<0.0001; **Fig. S8A**). This randomized axonal growth phenotype persisted in E6.5 embryos (Fig.7G, G', arrowheads) as opposed to control embryos (**Fig. 7F-F'**, arrows, **7I**; p<0.001), but at a significantly reduced degree as compared to E4.5 (**Fig. S8B**; p<0.05). To further validate the effect of FMRP knockout using the Crispr/Cas approach, we designed an additional set of guide RNAs (gRNA$_1$ and gRNA$_2$) to target exon 4 of FMRP (**Fig. S9A**). Electroporation of gRNA$_{1+2}$ plasmids demonstrated significant disorganized growth of NM-GFP$^+$ axons (p<0.05; **Fig. S9B-D**) as well as loss of FMRP immunoreactivity in the electroporated cells (**Fig. S9E-F)**. Together, these results indicate that FMRP is required for the directed growth of NM precursor axons in a tight dorsal-to-ventral fascicule.

In addition to the disoriented pattern of axonal growth, possibly due to axon defasciculation, fewer axons crossed and progressed to the contralateral side following FMRP knockout on flat-mount views of E4.5 embryos (**Fig. 7B, B'**). Observations from transverse sections confirmed that fewer axons reached the level of the floor plate (**Fig. 7E**, arrows). We evaluated the rate of midline crossing by calculating the ipsilateral/contralateral ratio of GFP^+ axons of the same transverse section, as described in Fig. 2D. At E4.5, the majority of GFP+ axons crossed the midline in control embryos, while only less than half extended contralaterally following FMRP knockout (**Fig. 7J**; $p<0.01$). Yet, two days later at E6.5, the majority of GFP+ axons had crossed the midline in $gRNA_{3+4}$ electroporated embryos (**Fig. 7G**, arrows), similar to control embryos (**Fig. 7F**, arrows; **Fig. 7K;** $p=0.645$). This observation demonstrates that FMRP knockout induces a delay in reaching the floor plate but maintains the ability to cross the midline.

FMRP knockdown induces axon growth defects. We next examined whether a partial reduction in FMRP expression affects the axonal growth pattern using a shRNA method. *Fmr1* and control (scrambled) shRNAs were cloned into a transposon-based vector system with a *Tol2* vector containing doxycycline (Dox) regulatory components and an EGFP reporter (Wang et al., 2018), enabling Dox-dependent temporal control of gene expression. We electroporated *Fmr1* and scrambled shRNA plasmids into E2.5 hindbrains, triggered shRNA expression with Dox treatment immediately following the electroporation, and fixed embryos at E4.5 and E6.5 (n=6-8 embryos for each plasmid at each stage). As expected, the scrambled-shRNA group exhibited the typical dA1 projecting pattern (**Fig. 8A-A'**, **C-C', F-F**' arrows). Embryos expressing *Fmr1*-shRNA, however, showed profoundly aberrant axons (**Fig. 8B, B'**, dashed-arrows), similar to the FMRP knockout effect. Transverse section views confirmed that many *Fmr1*-shRNA-$EGFP^+$ axons projected randomly toward the ventricular zone or toward the midline in a disorganized manner (**Fig. 8D-D'**, **E-E'**,**G-G'**, arrowheads), in high contrast to the organized and directional pattern in control embryos (**Fig. 8C-C'**,**F-F'**). The width of *Fmr1*-shRNA-GFP^+ axons was significantly larger than that of control axons at both E4.5 (**Fig. 8H**; $p<0.01$) and E6.5 (**Fig. 8I**; $p<0.05$). Nevertheless, similar to the effect of $gRNA_{3+4}$ expression, the degree of the axonal bundle width at E6.5 was reduced as compared to E4.5 (**Fig. S8C**; $p<0.05$). Two-way ANOVA analyses did not reveal a significant effect of either the type of FMRP manipulation ($F(1,29)=4.127$; $p=0.052$) or the developmental stage ($F(1,29)=1.176$; $p=0.287$) on the degree of FMRP deficiency induced changes in the width of the axon bundle. Different from FMRP knockout, the majority of axons following shRNA-induced FMRP knockdown appeared to cross the midline normally at E4.5 (**Fig. 8D, E**). The rate of midline crossing was not significantly

different between the groups at either developmental stage (**Fig. 8J, K;** E4.5: p=0.2403; E6.5: p=0.7209). Altogether, using two loss-of-function strategies we confirmed that FMRP expression in dA1 axons is required for the directional axonal growth in a defined fascicule while navigating through developing brains.

To further determine whether loss of FMRP impairs the organized axonal growth of NM precursor axons, we analyzed its effect *in vitro*. Following electroporation of $gRNA_{control}$ or $gRNA_{3+4}$ plasmids at E2.5 (n=12 embryos for each plasmid), hindbrains were isolated at E3.5, suspended into single cells, and incubated for 5 days. The cultures contained GFP^+ cells along with non-transfected hindbrain cells (**Fig. 9**). To monitor the dynamics of neurite outgrowth, cultures were traced by live imaging every 6 hours. Cells expressing $gRNA_{control}$ plasmid demonstrated a gradual extension and elongation of neurites (**Fig. 9A**, **C**, **E**, **G**; **Movie S1**). Strikingly, cells expressing $gRNA_{3+4}$ plasmid demonstrated neurite overgrowth accompanied by aberrant turning of axons and enhanced branching along the neurites and in their terminals (**Fig. 9B**, **D, F**,**H**,**I-L**; **Movie S2**). Quantification of the results (n=6 wells for each plasmid) confirmed a gradual increase in neurite branch point ($p<0.01$) and length (p<0.001) over time in both treatments (**Fig. 9M, N**). Yet the values differ greatly between the groups, as indicated for instance by the ~3.5 fold increase in neurite branch points and length in cells expressing $gRNA_{3+4}$ plasmid compared to control cells at day 4. These *in vitro* results demonstrate that axons tend to spread and branch more extensively in the absence of FMRP, further verifying that FMRP is required to control the axonal growth behavior of NM precursors.

FMRP deficiency induces synaptic projection errors of NM axons in NL

We next determined whether FMRP is required for presynaptic targeting by assessing the effects of FMRP downregulation on the pattern of synaptic connectivity of NM axons within NL. We electroporated E2 embryos with *Fmr1*-shRNA or control (scrambled) shRNA into NM precursors and triggered shRNA expression with Dox treatment at E8 (**Fig. 10A**). This late-onset expression preserved earlier developmental events of NM axons before NL neurons reach their final destination. During this time window, FMRP immunoreactivity was reduced 40-60% in NM cell bodies as we measured previously (Wang et al., 2018).

We first examined embryos at E15 (n=8 embryos for scrambled-shRNA and 9 for *Fmr1*-shRNA). A typical projection pattern of NM axons was seen in both groups: $EGFP^+$ axons arising from NM extended to both the ipsilateral and contralateral NL. In embryos expressing scrambled-shRNA, NM axons were restricted to the dorsal NL ipsilaterally and ventral NL contralaterally (**Fig. 10B,D**). In contrast, embryos expressing *Fmr1*-shRNA demonstrated $EGFP^+$ axons that projected beyond their assigned neuropil domain, extended through the cell

body layer, and terminated within the other domain (**Fig. 10C,E**). We measured the area containing EGFP$^+$ axons in each neuropil domain of the contralateral NL and calculated the dorsal/ventral ratio of this measure. This ratio was low in embryos expressing scrambled-shRNA, indicating a strong preference for ventral localization, and was significantly enhanced following *Fmr1*-shRNA transfection (p=0.0079; **Fig. 10G**), demonstrating abnormal axonal overshoot. This phenotype became insignificant at E19 (n=5 embryos; **Fig. 10F-G**), indicating that the effect of FMRP deficiency on axon targeting is stage-dependent.

We next wanted to examine whether the aberrant NM axons form synapses. By dye-filling individual NL neurons, we found that EGFP$^+$ axons were located immediately opposite to the dorsal dendrites of NL neurons (**Fig. 11A-A''**). These EGFP$^+$ axons were immunoreactive to synaptotagmin 2 (Syt2; **Fig. 11B-B''**), a presynaptic vesicle calcium sensor for neurotransmitter release. Together, these observations demonstrate that the aberrant NM axons form synapses.

Finally, we examined whether FMRP knockdown altered the morphological maturation of NM axonal terminals. In embryos expressing *Fmr1*-shRNA, the number of filopodia per EGFP$^+$ terminal is 0-2 at E15, similar to control as measured from Athoh1-mGFP labeled terminals (**Fig. 12**; p=0.5695).

Discussion

Using high-specificity genetic tools in chicken embryos, we uncovered an early onset of FMRP localization in developing axons of auditory neurons and demonstrated that cell autonomous FMRP expression is required for orderly and timely axonal navigation and synaptic targeting *in vivo* during discrete episodes of axon and circuit development.

FMRP in axon navigation

NM cells are born at E2-2.5 (Rubel et al., 1976). FMRP localization can be detected as early as E4 in developing axons of NM precursors, demonstrating that FMRP starts localizing in distal axons of NM precursors shortly after Fmr1 gene expression and axon genesis. This finding is consistent with FMRP localization in newly formed neurites of PC-12 cells (De Diego Otero et al., 2002) and axon growth cones of cultured mammalian neurons (Antar et al., 2006; Hengst et al., 2006; Jain and Welshhans, 2016). FMRP has also been identified in relatively mature axons as a component of Fragile X granules (FXGs) in postnatal mammalian brains (Christie et al., 2009; Chyung et al., 2018; Korsak et al., 2017; Shepard et al., 2020). FMRP puncta found in developing NM axons resemble these FXGs in size and density (Christie et al., 2009). However, the majority of FXGs in postnatal mouse brainstems contain the Fragile X related proteins (FXR1P and FXR2P) but not FMRP (Chyung et al., 2018). Whether this difference reflects interspecies variation or developmental stage dependency is yet to be determined.

Consistent with axon localization of FMRP during early development, FMRP deficiency in Atoh1/NM precursors results in widened axonal bundles due to randomized axonal growth instead of directional growing in a defined fascicule. It is known that axon fasciculation can be controlled at the level of axonal growth cones (Honig et al., 1998) and/or regulated by axon tension through shaft-shaft interactions (Šmít et al., 2017). Our *in vitro* results support a likely involvement of growth cone behaviors as absence of FMRP in NM precursor axons leads to excessively branched growth cones together with axonal overgrowth. Indeed, previous studies showed that FMRP loss enhances growth cone filopodia and attenuates growth cone collapse *in vitro* (Antar et al., 2006; Doers et al., 2014; Li et al., 2009), and these actions may involve FMRP regulation of cell adhesion and axon guidance cues. For example, FMRP colocalizes with Dscam mRNAs in cortical axons (Jain and Welshhans, 2016) and Dscam promotes axon fasciculation in the developing optic fiber (Bruce et al., 2017). Netrin mRNAs are associated with FMRP in HEK293 cells and was linked to axon extension phenotype in *dfmr1* knockout drosophila (Kang et al., 2019). Notably, netrin has a profound role in navigating commissural axons in the hindbrain and spinal cord in a tight bundle toward the midline (Moreno-Bravo et al., 2019; Serafini et al., 1996; Varadarajan et al., 2017; Yung et al., 2018). Notably, the degree of the aberrant projections decreases as development proceeds. The partial recovery in the axonal directionality may suggest that FMRP-deficient axons are capable to correct their growth pattern with time, as shown for instance in an ascending projection connecting specific cortical layers in Fmr1 knockout mice (Bureau et al., 2008). Yet, to fully decipher the fate of FMRP-deficient axons, advanced *in vivo* live imaging techniques will be needed to trace the behavior of individual axons.

The second phenotype we identified is a delay in axonal midline crossing. In control embryos, axons of Atoh1/NM precursors crossed the midline at E4.5. Following FMRP knockout, the axon crossing was not complete until two days later at E6.5. This phenotype may be caused by a general slowing down of axon growth *in vivo*. For example, FXS neurons derived from human pluripotent stem cells show reduced neurite outgrowth (Doers et al., 2014). FMRP knockdown significantly reduces axonal growth of cultured mouse neurons in response to nerve growth factor (Wang et al., 2015b). This slowed growth may be partially associated with FMRP regulation of microtubule signaling and dynamics (Bodaleo and Gonzalez-Billault, 2016; Wang et al., 2015b). Alternatively, a delay in midline crossing could be secondary to axon defasciculation. In the zebrafish forebrain, axon-axon interaction (likely axon fasciculation) shapes the midline kinetics of commissural axons (Bak and Fraser, 2003). Moreover, overgrowth and overbranching of axons in brains of *Drosophila* FMRP mutants were reported

(Pan et al., 2004), consistent with our *in vitro* data in which rather than attenuation in axonal growth we observed extensive neurite growth and enhanced branching points upon FMRP knockout. Reduced axon fasciculation thus may negatively affect midline crossing in auditory neurons. However, a delay in midline crossing was not detected following FMRP knockdown, although FMRP knockdown results in similar degrees of axon defasciculation as FMRP knockout. This, then, suggests that FMRP regulates multiple factors in controlling the speed of axon crossing. Additional mechanisms may include suppressed expression of axon guidance genes and compromised neuronal response to guidance cues following FMRP loss (Halevy et al., 2015; Li et al., 2009).

FMRP in synaptic targeting

In addition to controlling axon pathfinding, FMRP is also involved in determining the pattern of local axon projection in their target area. Following acute FMRP deficiency, NM axons terminate, and likely form functional synapse, on both the dorsal and ventral dendrites of the same NL neurons. This projection pattern is expected to negatively affect the accuracy of coincidence detection of NL neurons. This change can be interpreted as a compromised ability of developmental axon pruning, as seen in *Drosophila* FMRP mutants (Pan et al., 2004; Tessier and Broadie, 2008). Defective synaptic elimination and dendritic pruning have also been observed in brains of FXS individuals and FMRP knockout mice (Comery et al., 1997; Ivanco and Greenough, 2002; Jawaid et al., 2018) as well as in FMRP-reduced NM neurons (Wang et al., 2018). However, there is no evidence that NM axons normally project to both dendritic domains of the same NL neurons and subsequently retract from one domain (Young and Rubel, 1986; Rubel and Fritzsch, 2002). It is therefore likely that the aberrant axon projection following FMRP knockdown reflects errors in axon targeting. NM axons with less FMRP may become less sensitive to guiding cues from NL neurons or local astrocytes that control the pattern of synaptic distribution (Allen-Sharpley and Cramer, 2012; Korn et al., 2012; Rotschafer et al., 2016). This possibility is consistent with the localization of FMRP puncta in the distal axonal processes (Fig. 5). Although their exact relationship with synapses is yet to be determined, it is notable that many FMRP puncta are not in the region where synapses are located. Thus, FMRP is likely to exert its axonal functions that are identified in our study without being associated with synapses. Additional lines of evidence in support of FMRP regulation of axonal targeting vis growth cone dynamics include the presence of abnormal protein pattern only during the period when NM axons exhibit dynamic growth cones with filopodia and the normal maturation of axonal endings from growth cones to bouton-like terminals independent of FMRP expression.

It is worth to note that axon-glia interactions may also contribute to FMRP regulation of axon events, given their well-established roles in axon guidance, fasciculation, and targeting (Rigby et al., 2020). Interestingly, some of the molecules that participate in a direct axon-glia contact, such as NCAM and Semaphorins-Plexins (Franceschini and Barnett, 1996; Goldberg et al., 2004; Keilhauer et al., 1985; Miragall et al., 1989; Moreau-Fauvarque et al., 2003; Neugebauer et al., 1988; Shim et al., 2012), are known as FMRP targets in neurons (Li et al., 2009; Liao et al., 2008; Menon and Mihailescu, 2007). Hence, it is possible that lack of FMRP in NM axons prevents their interaction with glial cells via these proteins that in turn, leads to aberrant axonal growth. Additionally, FMRP may control axonal targeting by regulating the formation of axon myelination (Doll et al., 2020; Pacey et al., 2013) which influences functional development of axon terminals (Berret et al., 2016; Xu et al., 2017).

It remains unknown whether the tonotopic organization of NM axonal projection was affected by FMRP deficiency. Our manipulations affected only ~15% NM neurons that were often scattered throughout the cell group, thus unable to determine the effect on the tonotopic organization. Studies of *Fmr1* knockout mice demonstrated a normal tonotopic frequency representation in the auditory cortex (Kim et al., 2013). However, FMRP loss diminishes the developmental plasticity of this representation (Kim et al., 2013), flattens the tonotopic organization of potassium channel Kv3.1b (Strumbos et al., 2010), and results in frequency-specific decreases in inhibitory presynaptic structures (McCullagh et al., 2017), suggesting a potential link of FMRP with specific features of tonotopic regulations.

New insights in FXS pathogenesis

Our results enhances the current understanding of FXS pathogenesis in three aspects. First, we strengthen the concept that FXS neuropathology involves sensory systems. FMRP is strongly expressed in the auditory system (Zorio et al., 2017) and FMRP loss alters cellular properties of auditory neurons and auditory processing (reviewed in McCullagh et al., 2020). Our current and previous studies (Wang et al., 2018) further demonstrate a role of FMRP in the proper development of auditory connectivity. Second, we reveal a cell autonomous regulation of FMRP in axon navigation. Early-onset axon localization of FMRP suggests that this regulation occurs locally in axons, supporting axonal mechanisms of FXS pathology. For example, diffusion tensor imaging in FXS females revealed morphological changes in white matter tracts that may reflect alterations in axon density or coherence (Barnea-Goraly et al., 2003). Thus, FMRP loss-induced axon defasciculation may be a mechanism that underlies this clinical phenotype. Lastly, our results add to the existing literature that FMRP loss leads to substantial alterations in developing

brains that may be undetectable later in life. FMRP knockout mouse cortex shows alterations in connection probability, axon shape, and dendritic spine length at early, but not late postnatal ages (Bureau et al., 2008; Galvez and Greenough, 2005; Nimchinsky et al., 2001). Our current and previous studies further show developmentally restricted dendritic and axonal alterations in auditory neurons (Wang et al., 2018). The significance of these early-onset and transient changes was recently highlighted in *Drosophila*, in which the requirement of FMRP for normal brain function and behaviors is tightly restricted to an early developmental period (Doll and Broadie, 2015; Sears and Broadie, 2018). If this holds true in vertebrates, it would suggest that early axon deficits following FMRP loss may be responsible for life-long behavioral deficits in FXS. Although challenging, identifying FMRP regulation of early developmental events and determining how this regulation influences later circuit properties may be the beginning of a deeper understanding of FXS neuropathology. The auditory brainstem circuits and the novel genetic tools developed in this study provide a strategy that contributes to this effort.

Materials and Methods

Animals and *in ovo* electroporation

Fertilized White Leghorn and Loman Broiler chicken eggs (*Gallus gallus dometicus*) were obtained from Charles River Laboratories (Wilmington, MA, USA) and Gil-Guy Farm (Orot, Israel), respectively. Eggs were incubated for 2 to 2.5 days at 38°C until Hamburger Hamilton Stage 12-15. *In ovo* electroporation was performed as described previously (Kohl et al., 2012; Wang et al., 2018). Briefly, DNA constructs (4-5 µg/µl, diluted in phosphate-buffered saline [PBS]) were injected into the lumen of neural tubes at the rhombomere 5-6 level. Electroporation was performed with a platinum bipolar electrode or bent L-shaped gold electrodes that were placed on the two sides of the hindbrain to gain unilateral transfection. Embryos underwent 4 electrical pulses of 20-25 volts 30-45 ms in duration using a BTX 3000 (Harvard Apparatus, Cambridge, MA, USA) or a Grass SD9 electroporator (Grass instruments, Quincy, MA, USA). Following electroporation, the eggs were re-incubated until dissection at desired developmental stages. Embryos electroporated with drug inducible constructs (see below) were treated by adding 50 µl of doxycycline (1 mg/ml in sterile PBS; MilliporeSigma, St. Louis, MO, USA) onto the chorioallantoic membrane to trigger transgene transcription. Following the first Dox administration, embryos were treated again every other day to maintain gene expression before tissue dissection.

Hindbrain primary cultures and time lapse analysis

Hindbrains from electroporated embryos were dissected at E3.5 and incubated for 10 minutes at 37°C with TrypLE Express (Gibco, Thermo Fisher Scientific, Waltham, MA, USA) to dissociate the tissue into single cells, as previously described (Peretz et al., 2016; Peretz et al., 2018). TrypLE was neutralized with embryonic stem cell media containing DMEM/F-12 1:1, 20% KnockOut serum replacement, 2 mM GlutaMax L-alanyl-L-glutamine, 0.1 mM nonessential amino acids, and 1:50 penicillin-streptomycin (all from Gibco, Thermo Fisher Scientific), together with 0.1 mM β-mercaptoethanol and amphotericin B (1:400) (both from MilliporeSigma). Cells were passed through a 100 µm mesh strainer, centrifuged at 600 g for 10 minutes, seeded in 48-well plates (~2X10^5 cells/well) (Nunclon Delta Surface, Thermo Fisher Scientific), and incubated at 37°C in 5% CO2. For live imaging, well plates were imaged every 6 hours in the IncuCyte S3 Zoom HD/2CLR time-lapse microscopy system equipped with x 20_Plan Fluorobjective (Sartorius, Göttingen, Germany). Time-lapse movies were generated by capturing phase and green fluorescence images of cells in wells for up to 5 days. Stacks of images were exported in TIF format using the IncuCyte graph/export menu. Videos were assembled by exporting into MP4 format.

Plasmid construction

For genetic targeting of Atoh1 neurons, an Atoh1-enhancer element (Helms et al., 2000; Pennacchio et al., 2006) was cloned upstream to a Cre-recombinase sequence (Atoh1-Cre) and electroporated along with a conditional reporter plasmid containing a floxed STOP cassette in between the CAGG enhancer/promoter module and nuclear (n) or membranal (m) *GFP* gene (pCAGG-LoxP-STOP-LoxP-n/mGFP), as previously reported (Avraham et al., 2009; Kohl et al., 2012; Lumpkin et al., 2003; Reeber et al., 2008). For plasmid integration into the genome, the conditional reporter cassette was cloned between two PiggyBac (PB) arms (PB-CAGG-LoxP-STOPLoxPSTOP-GFP-PB) and electroporated along with the Atoh1-Cre and Pbase transposase plasmids (Hadas et al., 2014; Kohl et al., 2012; Lu et al., 2009; Wang et al., 2010). For tracing pre-synaptic connections, a reporter plasmid containing the synaptic tracer SV2-GFP (PB-CAG-LoxP-STOP-LoxP-SV2- GFP-PB) (Hadas et al., 2014; Kohl et al., 2012) was electroporated along with the Atoh1 enhancer and the Pbase transposase.

For constitutive expression of chicken or human *Fmr1*, mCherry-*Fmr1* fused coding sequence was chemically synthesized (GenScript, Piscataway, NJ) and sub-cloned into the pT2K-CAGGS vector. For electroporation, the two plasmids (pT2K-CAGGS-mCherry-chFMRP and pCAGGS-T2TP) were concentrated at 4-5 µg/µl and mixed at equal amounts.

For shRNA targeting of FMRP, five shRNAs directed against specific sequences of chicken *Fmr1* were designed using siRNA Wizard v3.1 (InvivoGen, San Diego, CA, USA) and the siDESIGN Center (Thermo Fisher Scientific). Plasmids were chemically synthesized (GENEWIZ, South Plainfield, NJ, USA) and endo free DNA Maxi Preps were performed (Qiagen, Hilden, Germany). The most effective shRNA (gaggatcaagatgcagtgaaata; nucleotides 951-973 of chicken *Fmr1*) was determined based on its knockdown effect in the developing brainstem (Wang et al., 2018) and used for subsequent experiments. A scrambled shRNA (attagaataagtgcgagagaata) was designed using the Genscript algorithm (Piscataway, NJ, USA) and confirmed by blasting this shRNA sequence against the chicken genome. *Fmr1* and scrambled shRNAs were cloned into a transposon-based vector system with a *Tol2* vector containing doxycycline regulatory components (Schecterson et al., 2012; Wang et al., 2018). Tol2 transposable element sequences enable stable integration of the transposon into the chick genome, whereas doxycycline regulatory elements allow temporal control of gene expression.

For Crispr/Cas9 targeting of FMRP, we used the Genome Engineering Toolbox that was designed by the Zhang lab (Cong et al., 2013). The pX330 plasmid (addgene) (Sakuma et al., 2014) was modified by adding a T2A-EGFP cassette at the carboxyl terminus of Cas9. gRNAs to *Fmr1* were designed utilizing the chopchop design tool (https://chopchop.cbu.uib.no/). gRNAs targeting exon 8 were cloned into the modified pX330 plasmid (Table 1). For testing the efficiency of the gRNA, the targeting plasmids were electroporated into the hindbrain at E2.5. Hindbrains were dissected 48 hours following electroporation, and a 2 mm hindbrain tissue was processed for DNA extraction, using ‘tail digestion and DNA extraction’ protocol (Wang and Storm, 2006). Genomic DNA was analyzed by polymerase chain reaction (PCR) using primers specific to sequences up- and down-stream of the FMRP-gRNA$_{3+4}$ target sites. Nested PCR was used to amplify the targeted region. For exon 8 targeting, Test-F3 and Test-R1 were used for the first round of PCR, followed by Test-F2 and Test-R2 for the second round.

Staining and immunocytochemistry

Brainstem was dissected at various stages and immersed in 4% paraformaldehyde in 0.1 M phosphate buffer (PB) overnight at 4°C. For whole mount preparation, hindbrains were cut open along the roof plate, after which the tissue was spread open on slides to produce flat-mount preparations (Kayam et al., 2013; Weisinger et al., 2012). For transverse sections, brainstems were transferred to 30% sucrose in PB until settling, followed by their sectioning in the coronal plane at 30 µm. Alternate sections were immunohistochemically stained by incubation with primary antibody solutions diluted in PBS with 0.3% Triton X-100 overnight at 4°C, followed by

Alexa-Fluor secondary antibodies (Life Technologies, Carlsbad, CA, USA) at 1:1000 overnight at 4°C. Some sections were counterstained with DAPI and/or NeuroTrace (Life Technologies), a fluorescent Nissl stain, at a concentration of 1:1000 and incubated together with secondary antibodies. Sections were mounted on gelatin-coated slides and coverslipped with Fluoromount-G mounting medium® (Southern Biotech, Birmingham, AL, USA) for imaging.

Primary antibodies used include the custom-made polyclonal rabbit anti-FMRP (Wang et al., 2018; Yu et al., 2020), anti-Synaptotagmin 2 (1:1000, DSHB Cat# znp-1, RRID: AB_2315626), anti-SNAP25 (1:1000, Abcam Cat# 5666, RRID: AB_305033), anti-microtubule associated protein 2 (MAP2; Milipore, Burlington, MA, USA; #MAB 3418; RRID: AB_94856), custom-made polyclonal rabbit anti-Lhx2/9 (1:100, I. Sibony and T.Schultheiss, unpublished data; kind gift from T. Schultheiss, Technion-Israel Institute of Technology, Haifa, Israel), and polyclonal rabbit anti VGluT2 (1:150, Synaptic Systems, Göttingen, Germany; CAT# 135402,)

Single-cell filling

Following electroporation with *Fmr1*-shRNA plasmids and doxycycline treatment, E15 embryos were used to prepare acute brainstem slices as previously described (Wang et al., 2017). NL cells were individually dye-filled with Alexa Fluro 568 dextran (Invitrogen) following our published protocol (Wang and Rubel, 2012; Wang et al., 2017).

Data analysis

Quantification of Atoh1-Cre NM ratio. Atoh1-Cre transfected NM neurons and total NM neurons counterstained by NeuroTrace on each section were counted using Cell Counter of Image J. Sections from the same animal were grouped, and the transfection ratio was calculated as: transfection ratio = number of Atoh1-mGFP^{+} NM neurons / total NM neurons (n=8 embryos).

Quantification of axon terminal morphology. The axon terminal morphology was characterized by numbers of filopodia. Image stacks containing identifiable intact axon terminals were reconstructed using image J, and the numbers of filopodia on each terminal were counted on both ipsilateral and contralateral sides. Number of filopodium per terminal was then calculated and compared between the immature stages (E11-E13) and E15.

Localization analysis of FMRP granule. FMRP granules localization in Atoh1-mGFP labeled axons were analyzed using Image J. Briefly, a straight-line ROI was drawn across a FMRP granule with Atoh1-mGFP transfection and applied to both channels respectively. The fluorescent intensity profile was then analyzed and plotted using GraphPad Prism 7 software.
Quantification of gRNA expressing cells. Quantification of expression of $gRNA_{control}$ and $gRNA_{3+4}$ plasmids in dA1 cells is demonstrated by Box plot analysis. For each group, two transverse sections obtained from 3 different embryos at E4.5 were taken. Each data point represents one section. The ratio of cells that co-express gRNA-GFP^+ and the dA1-specific marker Lhx2/9 out of the total gRNA-GFP^+ expressing cells is presented.

Quantification of FMRP expression. Quantification of the extent of FMRP expression in $gRNA_{control}$ and $gRNA_{3+4}$ expressing cells is demonstrated by Box plot analysis. For each group, electroporated sagittal sections obtained from 7 different embryos at E6 were taken. Each data point represents one section for which the ratio of ($FMRP^+$+GFP^+)/GFP^+ cells was measured.

Quantification of gRNA expressing cells. Quantification of expression of $gRNA_{control}$ and $gRNA_{3+4}$ plasmids in dA1 cells is demonstrated by Box plot analysis. For each group, two transverse sections obtained from 3 different embryos at E4.5 were taken. Each data point represents one section. The ratio of cells that co-express gRNA-GFP^+ and the dA1-specific marker Lhx2/9 out of the total gRNA-GFP^+ expressing cells is presented.

Quantification of axon fascicule width. Axonal width measurement was performed for 2 different experiments (Fmr1-shRNA and FMRP-Crispr) at E4.5 and E6.5. Each stage included 2 groups: (1) $gRNA_{control}$ and $gRNA_{3+4}$ expressing cells and (2) sc-shRNA-GFP and Fmr1-shRNA-GFP expressing cells. Box plots are demonstrated for each group, from which cross sections from 7 different embryos (E4.5) or 4 embryos (E6.5) were taken. Each data point represents one section for which the ratio of the axonal length related to the mantle-ventricular width was measured using ImageJ software.

Quantification of axonal crossing. Box plot quantification of axonal crossing was performed for 2 different experiments at E4.5 and E6.5. Each stage contained 2 groups: (1) $gRNA_{control}$ and $gRNA_{3+4}$ expressing cells and (2) sc-shRNA-GFP and FMR1-shRNA-GFP expressing cells. For each group, cross sections from 7 different embryos (E4.5) or 4 embryos (E6.5) were taken. Each data point represents one section for which the ratio of the signal intensity between commissural axons and non-commissural axons was measured using ImageJ software.

Quantification of neurite length and branch points in cultures. Neurite length (mm/mm^2) and branch point (per mm^2) were calculated in $gRNA_{control}$ and $gRNA_{3+4}$ expressing neurons in each well (n=6 wells for each treatment) using the IncuCyte Zoom NeuroTrack software module (Sartorius, USA), as described in (Wurster et al., 2019). Microplate graphs were generated using the time plot feature in the graph/export menu of the IncuCyte Zoom software.

Quantification of Atoh1-Cre expressing cells. Percentage of Atoh1-Cre::nGFP expressing cells was calculated by counting the number of GFP^+ nuclei that co-express the dA1-specific marker Lhx2/9 out of the total GFP-expressing nuclei (n=7 embryos).

Quantification of the laminar specificity of axon targeting. Axonal projection was measured from Fmr1-shRNA transfected embryos at E15 and E19, as well as from scrambled-shRNA transfected embryos at E15 using Image J. For each embryo, transverse sections containing the middle and rostral NL where NL cell bodies are aligned into a single layer were used for the analysis. For each section, the dorsal and ventral neuropil regions of NL on the side contralateral to the transfection were outlined based on NeuroTrace staining. The neuropil area covered by $EGFP^+$ axons was then measured for each neuropil region. The specificity of axon projection was evaluated by calculating the ratio of the dorsal $EGFP^+$ area to the ventral $EGFP^+$ area. The ratios from all sections (usually 2-3) of the same embryo were averaged as individual data points and compared between Fmr1-shRNA and control-shRNA transfected animals (n=5-9 animals for each group).

Statistics. Statistics were performed by Mann-Whitney non-parametric test using the Graphpad Prism 7 software package (GraphPad Software, La Jolla, CA, USA). $p < 0.05$ was considered statistically significant. Data were displayed as mean $\pm$ SD or SEM as indicated in the Results. Each individual data point represents one animal. Two-way ANOVA was used for Tukey multiple comparisons.

Acknowledgements

We thank Edwin W Rubel (University of Washington) for facilitating the collaboration between YW and DSD. We are grateful to David Fradkin for his assistance with the IncuCyte system, Itzhak Sibony and Tom Schultheiss for the Lhx2/9 antibody, and Daniel Lazar for her help with the tissue culture.

Competing interests

No competing interests declared.

Funding

This work was supported by the National Institutes of Health (DC13074 and DC17267 to Y. W.), the United States – Israel Binational Science Foundation (2015087 to Y.W. and D.S.), The Israel Science Foundation (1515/16 to D.S) and The Chief Scientist Office, Ministry of Health (3-0000-33793 to D.S).

Data Availability

None.

References

Abitbol, M., Menini, C., Delezoide, A. L., Rhyner, T., Vekemans, M. and Mallet, J. (1993). Nucleus basalis magnocellularis and hippocampus are the major sites of FMR-1 expression in the human fetal brain. *Nat. Genet.* 4, 147–153.

Allen-Sharpley, M. R. and Cramer, K. S. (2012). Coordinated Eph-ephrin signaling guides migration and axon targeting in the avian auditory system. *Neural Dev* 7, 29.

Antar, L. N., Li, C., Zhang, H., Carroll, R. C. and Bassell, G. J. (2006). Local functions for FMRP in axon growth cone motility and activity-dependent regulation of filopodia and spine synapses. *Molecular and Cellular Neuroscience* 32, 37–48.

Avraham, O., Hadas, Y., Vald, L., Zisman, S., Schejter, A., Visel, A. and Avihu, K. (2009). Transcriptional control of axonal guidance and sorting in dorsal interneurons by the Lim-HD proteins Lhx9 and Lhx1. *Neural Dev* 4, 21.

Bagni, C. and Greenough, W. T. (2005). From mRNP trafficking to spine dysmorphogenesis: the roots of fragile X syndrome. *Nat. Rev. Neurosci.* 6, 376–387.

Bagni, C. and Zukin, R. S. (2019). A Synaptic Perspective of Fragile X Syndrome and Autism Spectrum Disorders. *Neuron* 101, 1070–1088.

Bak, M. and Fraser, S. E. (2003). Axon fasciculation and differences in midline kinetics between pioneer and follower axons within commissural fascicles. *Development* 130, 4999–5008.

Barnea-Goraly, N., Eliez, S., Hedeus, M., Menon, V., White, C. D., Moseley, M. and Reiss, A. L. (2003). White matter tract alterations in fragile X syndrome: Preliminary evidence from diffusion tensor imaging. *Am. J. Med. Genet.* 118B, 81–88.

Bassell, G. J. and Warren, S. T. (2008). Fragile X Syndrome: Loss of Local mRNA Regulation Alters Synaptic Development and Function. *Neuron* 60, 201–214.

Bear, M. F., Huber, K. M. and Warren, S. T. (2004). The mGluR theory of fragile X mental retardation. *Trends Neurosci.* 27, 370–377.

Bermingham, N. A., Hassan, B. A., Wang, V. Y., Fernandez, M., Banfi, S., Bellen, H. J., Fritzsch, B. and Zoghbi, H. Y. (2001). Proprioceptor pathway development is dependent on Math1. *Neuron* 30, 411–422.

Berret, E., Kim, S. E., Lee, S. Y., Kushmerick, C. and Kim, J. H. (2016). Functional and structural properties of ion channels at the nerve terminal depends on compact myelin: Ion channels at the CNS nerve terminal. *J. Physiol.* 594, 5593–5609.

Bodaleo, F. J. and Gonzalez-Billault, C. (2016). The Presynaptic Microtubule Cytoskeleton in Physiological and Pathological Conditions: Lessons from Drosophila Fragile X Syndrome and Hereditary Spastic Paraplegias. *Front Mol Neurosci* 9, 60.

Brown, M. R., Kronengold, J., Gazula, V.-R., Chen, Y., Strumbos, J. G., Sigworth, F. J., Navaratnam, D. and Kaczmarek, L. K. (2010). Fragile X mental retardation protein controls gating of the sodium-activated potassium channel Slack. *Nat Neurosci* 13, 819–821.

Bruce, F. M., Brown, S., Smith, J. N., Fuerst, P. G. and Erskine, L. (2017). DSCAM promotes axon fasciculation and growth in the developing optic pathway. *Proc. Natl. Acad. Sci. U.S.A.* 114, 1702–1707.

Bureau, I., Shepherd, G. M. G. and Svoboda, K. (2008). Circuit and Plasticity Defects in the Developing Somatosensory Cortex of Fmr1 Knock-Out Mice. *Journal of Neuroscience* 28, 5178–5188.

Castrén, M. L. (2016). Cortical neurogenesis in fragile X syndrome. *Front Biosci* 8, 160–168.

Chédotal, A. and Richards, L. J. (2010). Wiring the Brain: The Biology of Neuronal Guidance. *Cold Spring Harbor Perspectives in Biology* 2, a001917–a001917.

Christie, S. B., Akins, M. R., Schwob, J. E. and Fallon, J. R. (2009). The FXG: a presynaptic fragile X granule expressed in a subset of developing brain circuits. *J. Neurosci.* 29, 1514–1524.

Chyung, E., LeBlanc, H. F., Fallon, J. R. and Akins, M. R. (2018). Fragile X granules are a family of axonal ribonucleoprotein particles with circuit-dependent protein composition and mRNA cargos. *J Comp Neurol* 526, 96–108.

Comer, J. D., Alvarez, S., Butler, S. J. and Kaltschmidt, J. A. (2019). Commissural axon guidance in the developing spinal cord: from Cajal to the present day. *Neural Dev* 14, 9.

Comery, T. A., Harris, J. B., Willems, P. J., Oostra, B. A., Irwin, S. A., Weiler, I. J. and Greenough, W. T. (1997). Abnormal dendritic spines in fragile X knockout mice: maturation and pruning deficits. *Proc. Natl. Acad. Sci. U.S.A.* 94, 5401–5404.

Cong, L., Ran, F. A., Cox, D., Lin, S., Barretto, R., Habib, N., Hsu, P. D., Wu, X., Jiang, W., Marraffini, L. A., et al. (2013). Multiplex genome engineering using CRISPR/Cas systems. *Science* 339, 819–823.

Cramer, K. S., Fraser, S. E. and Rubel, E. W. (2000). Embryonic Origins of Auditory Brain-Stem Nuclei in the Chick Hindbrain. *Developmental Biology* 224, 138–151.

Cramer, K. S., Bermingham-McDonogh, O., Krull, C. E. and Rubel, E. W. (2004). EphA4 signaling promotes axon segregation in the developing auditory system. *Developmental Biology* 269, 26–35.

Davis, J. K. and Broadie, K. (2017). Multifarious Functions of the Fragile X Mental Retardation Protein. *Trends Genet.* 33, 703–714.

De Diego Otero, Y., Severijnen, L.-A., van Cappellen, G., Schrier, M., Oostra, B. and Willemsen, R. (2002). Transport of fragile X mental retardation protein via granules in neurites of PC12 cells. Mol. Cell. Biol. 22, 8332–8341.

Deng, P.-Y., Rotman, Z., Blundon, J. A., Cho, Y., Cui, J., Cavalli, V., Zakharenko, S. S. and Klyachko, V. A. (2013). FMRP regulates neurotransmitter release and synaptic information transmission by modulating action potential duration via BK channels. *Neuron* 77, 696–711.

Doers, M. E., Musser, M. T., Nichol, R., Berndt, E. R., Baker, M., Gomez, T. M., Zhang, S.-C., Abbeduto, L. and Bhattacharyya, A. (2014). iPSC-derived forebrain neurons from FXS individuals show defects in initial neurite outgrowth. *Stem Cells Dev.* 23, 1777–1787.

Doll, C. A. and Broadie, K. (2015). Activity-dependent FMRP requirements in development of the neural circuitry of learning and memory. *Development* 142, 1346–1356.

Doll, C. A., Yergert, K. M. and Appel, B. H. (2020). The RNA binding protein fragile X mental retardation protein promotes myelin sheath growth. *Glia* 68, 495–508.

El-Hassar, L., Song, L., Tan, W. J. T., Large, C. H., Alvaro, G., Santos-Sacchi, J. and Kaczmarek, L. K. (2019). Modulators of Kv3 Potassium Channels Rescue the Auditory Function of Fragile X Mice. *J. Neurosci.* 39, 4797–4813.

Farago, A. F., Awatramani, R. B. and Dymecki, S. M. (2006). Assembly of the Brainstem Cochlear Nuclear Complex Is Revealed by Intersectional and Subtractive Genetic Fate Maps. *Neuron* 50, 205–218.

Farzin, F., Rivera, S. M. and Whitney, D. (2011). Resolution of spatial and temporal visual attention in infants with fragile X syndrome. *Brain* 134, 3355–3368.

Ferron, L., Nieto-Rostro, M., Cassidy, J. S. and Dolphin, A. C. (2014). Fragile X mental retardation protein controls synaptic vesicle exocytosis by modulating N-type calcium channel density. *Nat Commun* 5, 3628.

Franceschini, I. A. and Barnett, S. C. (1996). Low-affinity NGF-receptor and E-N-CAM expression define two types of olfactory nerve ensheathing cells that share a common lineage. *Dev. Biol.* 173, 327–343.

Fujiyama, T., Yamada, M., Terao, M., Terashima, T., Hioki, H., Inoue, Y. U., Inoue, T., Masuyama, N., Obata, K., Yanagawa, Y., et al. (2009). Inhibitory and excitatory subtypes of cochlear nucleus neurons are defined by distinct bHLH transcription factors, Ptf1a and Atoh1. *Development* 136, 2049–2058.

Galvez, R. and Greenough, W. T. (2005). Sequence of abnormal dendritic spine development in primary somatosensory cortex of a mouse model of the fragile X mental retardation syndrome. *Am. J. Med. Genet. A* 135, 155–160.

Garcia-Pino, E., Gessele, N. and Koch, U. (2017). Enhanced Excitatory Connectivity and Disturbed Sound Processing in the Auditory Brainstem of Fragile X Mice. *J. Neurosci.* 37, 7403–7419.

Goldberg, J. L., Vargas, M. E., Wang, J. T., Mandemakers, W., Oster, S. F., Sretavan, D. W. and Barres, B. A. (2004). An oligodendrocyte lineage-specific semaphorin, Sema5A, inhibits axon growth by retinal ganglion cells. *J. Neurosci.* 24, 4989–4999.

Gray, P. A. (2013). Transcription factors define the neuroanatomical organization of the medullary reticular formation. *Front Neuroanat* 7, 7.

Hadas, Y., Etlin, A., Falk, H., Avraham, O., Kobiler, O., Panet, A., Lev-Tov, A. and Klar, A. (2014). A ‘tool box’ for deciphering neuronal circuits in the developing chick spinal cord. *Nucleic Acids Research* 42, e148–e148.

Hagerman, R. J., Berry-Kravis, E., Hazlett, H. C., Bailey, D. B., Moine, H., Kooy, R. F., Tassone, F., Gantois, I., Sonenberg, N., Mandel, J. L., et al. (2017). Fragile X syndrome. *Nat Rev Dis Primers* 3, 17065.

Halevy, T., Czech, C. and Benvenisty, N. (2015). Molecular mechanisms regulating the defects in fragile X syndrome neurons derived from human pluripotent stem cells. *Stem Cell Reports* 4, 37–46.

Hall, S. S., Walter, E., Sherman, E., Hoeft, F. and Reiss, A. L. (2009). The neural basis of auditory temporal discrimination in girls with fragile X syndrome. *J Neurodevelop Disord* 1, 91–99.

Helms, A. W., Abney, A. L., Ben-Arie, N., Zoghbi, H. Y. and Johnson, J. E. (2000). Autoregulation and multiple enhancers control Math1 expression in the developing nervous system. *Development* 127, 1185–1196.

Hendricks, S. J., Rubel, E. W. and Nishi, R. (2006). Formation of the avian nucleus magnocellularis from the auditory anlage. *J. Comp. Neurol.* 498, 433–442.

Hengst, U., Cox, L. J., Macosko, E. Z. and Jaffrey, S. R. (2006). Functional and selective RNA interference in developing axons and growth cones. *J. Neurosci.* 26, 5727–5732.

Hille, F. and Charpentier, E. (2016). CRISPR-Cas: biology, mechanisms and relevance. *Phil. Trans. R. Soc. B* 371, 20150496.

Hinds, H. L., Ashley, C. T., Sutcliffe, J. S., Nelson, D. L., Warren, S. T., Housman, D. E. and Schalling, M. (1993). Tissue specific expression of FMR-1 provides evidence for a functional role in fragile X syndrome. *Nat. Genet.* 3, 36–43.

Honig, M. G., Petersen, G. G., Rutishauser, U. S. and Camilli, S. J. (1998). In vitro studies of growth cone behavior support a role for fasciculation mediated by cell adhesion molecules in sensory axon guidance during development. *Dev. Biol.* 204, 317–326.

Ivanco, T. L. and Greenough, W. T. (2002). Altered mossy fiber distributions in adultFmr1 (FVB) knockout mice. *Hippocampus* 12, 47–54.

Jain, S. and Welshhans, K. (2016). Netrin-1 induces local translation of down syndrome cell adhesion molecule in axonal growth cones: Local Translation of Dscam. *Devel Neurobio* 76, 799–816.

Jawaid, S., Kidd, G. J., Wang, J., Swetlik, C., Dutta, R. and Trapp, B. D. (2018). Alterations in CA1 hippocampal synapses in a mouse model of fragile X syndrome. *Glia* 66, 789–800.

Kang, H., Zhao, J., Jiang, X., Li, G., Huang, W., Cheng, H. and Duan, R. (2019). Drosophila Netrin-B controls mushroom body axon extension and regulates courtship-associated learning and memory of a Drosophila fragile X syndrome model. *Mol Brain* 12, 52.

Kayam, G., Kohl, A., Magen, Z., Peretz, Y., Weisinger, K., Bar, A., Novikov, O., Brodski, C. and Sela-Donenfeld, D. (2013). A novel role for Pax6 in the segmental organization of the hindbrain. *Development* 140, 2190–2202.

Keilhauer, G., Faissner, A. and Schachner, M. (1985). Differential inhibition of neurone-neurone, neurone-astrocyte and astrocyte-astrocyte adhesion by L1, L2 and N-CAM antibodies. *Nature* 316, 728–730.

Kéri, S. and Benedek, G. (2011). Fragile X protein expression is linked to visual functions in healthy male volunteers. *Neuroscience* 192, 345–350.

Kim, H., Gibboni, R., Kirkhart, C. and Bao, S. (2013). Impaired critical period plasticity in primary auditory cortex of fragile X model mice. *J. Neurosci.* 33, 15686–15692.

Kogan, C. S., Bertone, A., Cornish, K., Boutet, I., Der Kaloustian, V. M., Andermann, E., Faubert, J. and Chaudhuri, A. (2004). Integrative cortical dysfunction and pervasive motion perception deficit in fragile X syndrome. *Neurology* 63, 1634–1639.

Kohl, A., Hadas, Y., Klar, A. and Sela-Donenfeld, D. (2012). Axonal Patterns and Targets of dA1 Interneurons in the Chick Hindbrain. *Journal of Neuroscience* 32, 5757–5771.

Kohl, A., Hadas, Y., Klar, A. and Sela-Donenfeld, D. (2013). Electroporation of the Hindbrain to Trace Axonal Trajectories and Synaptic Targets in the Chick Embryo. *JoVE* 50136.

Kohl, A., Marquardt, T., Klar, A. and Sela-Donenfeld, D. (2015). Control of Axon Guidance and Neurotransmitter Phenotype of dB1 Hindbrain Interneurons by Lim-HD Code. *Journal of Neuroscience* 35, 2596–2611.

Korn, M. J., Koppel, S. J., Li, L. H., Mehta, D., Mehta, S. B., Seidl, A. H. and Cramer, K. S. (2012). Astrocyte-secreted factors modulate the developmental distribution of inhibitory synapses in nucleus laminaris of the avian auditory brainstem. *J. Comp. Neurol.* 520, 1262–1277.

Korsak, L. I. T., Shepard, K. A. and Akins, M. R. (2017). Cell type-dependent axonal localization of translational regulators and mRNA in mouse peripheral olfactory neurons. *J Comp Neurol* 525, 2202–2215.

Li, C., Bassell, G. and Sasaki, Y. (2009). Fragile X Mental Retardation Protein is involved in protein synthesis-dependent collapse of growth cones induced by Semaphorin-3A. *Front. Neural Circuits* 3,.

Liao, L., Park, S. K., Xu, T., Vanderklish, P. and Yates, J. R. (2008). Quantitative proteomic analysis of primary neurons reveals diverse changes in synaptic protein content in *fmr1* knockout mice. *PNAS* 105, 15281–15286.

Lipovsek, M. and Wingate, R. J. (2018). Conserved and divergent development of brainstem vestibular and auditory nuclei. *eLife* 7, e40232.

Lu, Y. (2019). Subtle differences in synaptic transmission in medial nucleus of trapezoid body neurons between wild-type and Fmr1 knockout mice. *Brain Research* 1717, 95–103.

Lu, Y., Lin, C. and Wang, X. (2009). PiggyBac transgenic strategies in the developing chicken spinal cord. *Nucleic Acids Res.* 37, e141.

Lumpkin, E. A., Collisson, T., Parab, P., Omer-Abdalla, A., Haeberle, H., Chen, P., Doetzlhofer, A., White, P., Groves, A., Segil, N., et al. (2003). Math1-driven GFP expression in the developing nervous system of transgenic mice. *Gene Expr. Patterns* 3, 389–395.

Machold, R. and Fishell, G. (2005). Math1 Is Expressed in Temporally Discrete Pools of Cerebellar Rhombic-Lip Neural Progenitors. *Neuron* 48, 17–24.

Maricich, S. M., Xia, A., Mathes, E. L., Wang, V. Y., Oghalai, J. S., Fritzsch, B. and Zoghbi, H. Y. (2009). Atoh1-Lineal Neurons Are Required for Hearing and for the Survival of Neurons in the Spiral Ganglion and Brainstem Accessory Auditory Nuclei. *Journal of Neuroscience* 29, 11123–11133.

McCullagh, E. A., Salcedo, E., Huntsman, M. M. and Klug, A. (2017). Tonotopic alterations in inhibitory input to the medial nucleus of the trapezoid body in a mouse model of Fragile X syndrome. *J Comp Neurol* 525, 3543–3562.

McCullagh, E. A., Rotschafer, S. E., Auerbach, B. D., Klug, A., Kaczmarek, L. K., Cramer, K. S., Kulesza, R. J., Razak, K. A., Lovelace, J. W., Lu, Y., et al. (2020). Mechanisms underlying auditory processing deficits in Fragile X syndrome. *FASEB J.*

Menon, L. and Mihailescu, M.-R. (2007). Interactions of the G quartet forming semaphorin 3F RNA with the RGG box domain of the fragile X protein family. *Nucleic Acids Res.* 35, 5379–5392.

Miragall, F., Kadmon, G. and Schachner, M. (1989). Expression of L1 and N-CAM cell adhesion molecules during development of the mouse olfactory system. *Dev. Biol.* 135, 272–286.

Moreau-Fauvarque, C., Kumanogoh, A., Camand, E., Jaillard, C., Barbin, G., Boquet, I., Love, C., Jones, E. Y., Kikutani, H., Lubetzki, C., et al. (2003). The transmembrane semaphorin Sema4D/CD100, an inhibitor of axonal growth, is expressed on oligodendrocytes and upregulated after CNS lesion. *J. Neurosci.* 23, 9229–9239.

Moreno-Bravo, J. A., Roig Puiggros, S., Mehlen, P. and Chédotal, A. (2019). Synergistic Activity of Floor-Plate- and Ventricular-Zone-Derived Netrin-1 in Spinal Cord Commissural Axon Guidance. *Neuron* 101, 625-634.e3.

Neugebauer, K. M., Tomaselli, K. J., Lilien, J. and Reichardt, L. F. (1988). N-cadherin, NCAM, and integrins promote retinal neurite outgrowth on astrocytes in vitro. *J. Cell Biol.* 107, 1177–1187.

Nimchinsky, E. A., Oberlander, A. M. and Svoboda, K. (2001). Abnormal development of dendritic spines in FMR1 knock-out mice. *J. Neurosci.* 21, 5139–5146.

Nothwang, H. G. (2016). Evolution of mammalian sound localization circuits: A developmental perspective. *Progress in Neurobiology* 141, 1–24.

Overholt, E. M., Rubel, E. W. and Hyson, R. L. (1992). A circuit for coding interaural time differences in the chick brainstem. *J. Neurosci.* 12, 1698–1708.

Pacey, L. K. K., Xuan, I. C. Y., Guan, S., Sussman, D., Henkelman, R. M., Chen, Y., Thomsen, C. and Hampson, D. R. (2013). Delayed myelination in a mouse model of fragile X syndrome. *Hum. Mol. Genet.* 22, 3920–3930.

Pan, L., Zhang, Y. Q., Woodruff, E. and Broadie, K. (2004). The Drosophila fragile X gene negatively regulates neuronal elaboration and synaptic differentiation. *Curr. Biol.* 14, 1863–1870.

Parvin, S., Takeda, R., Sugiura, Y., Neyazaki, M., Nogi, T. and Sasaki, Y. (2019). Fragile X mental retardation protein regulates accumulation of the active zone protein Munc18-1 in presynapses via local translation in axons during synaptogenesis. *Neuroscience Research* 146, 36–47.

Patel, A. B., Hays, S. A., Bureau, I., Huber, K. M. and Gibson, J. R. (2013). A target cell-specific role for presynaptic Fmr1 in regulating glutamate release onto neocortical fast-spiking inhibitory neurons. *J. Neurosci.* 33, 2593–2604.

Pennacchio, L. A., Ahituv, N., Moses, A. M., Prabhakar, S., Nobrega, M. A., Shoukry, M., Minovitsky, S., Dubchak, I., Holt, A., Lewis, K. D., et al. (2006). In vivo enhancer analysis of human conserved non-coding sequences. *Nature* 444, 499–502.

Peretz, Y., Eren, N., Kohl, A., Hen, G., Yaniv, K., Weisinger, K., Cinnamon, Y. and Sela-Donenfeld, D. (2016). A new role of hindbrain boundaries as pools of neural stem/progenitor cells regulated by Sox2. *BMC Biol* 14, 57.

Peretz, Y., Kohl, A., Slutsky, N., Komlos, M., Varshavsky, S. and Sela-Donenfeld, D. (2018). Neural stem cells deriving from chick embryonic hindbrain recapitulate hindbrain development in culture. *Sci Rep* 8, 13920.

Price, D. K., Zhang, F., Ashley, C. T. and Warren, S. T. (1996). The chicken FMR1 gene is highly conserved with a CCT 5'-untranslated repeat and encodes an RNA-binding protein. *Genomics* 31, 3–12.

Rais, M., Binder, D. K., Razak, K. A. and Ethell, I. M. (2018). Sensory Processing Phenotypes in Fragile X Syndrome. *ASN Neuro* 10, 1759091418801092.

Reeber, S. L., Sakai, N., Nakada, Y., Dumas, J., Dobrenis, K., Johnson, J. E. and Kaprielian, Z. (2008). Manipulating Robo expression in vivo perturbs commissural axon pathfinding in the chick spinal cord. *J. Neurosci.* 28, 8698–8708.

Rigby, M. J., Gomez, T. M. and Puglielli, L. (2020). Glial Cell-Axonal Growth Cone Interactions in Neurodevelopment and Regeneration. *Front Neurosci* 14, 203.

Rotschafer, S. E., Marshak, S. and Cramer, K. S. (2015). Deletion of Fmr1 Alters Function and Synaptic Inputs in the Auditory Brainstem. *PLoS ONE* 10, e0117266.

Rotschafer, S. E., Allen-Sharpley, M. R. and Cramer, K. S. (2016). Axonal Cleaved Caspase-3 Regulates Axon Targeting and Morphogenesis in the Developing Auditory Brainstem. *Front. Neural Circuits* 10,.

Rubel, E. W. and Fritzsch, B. (2002). Auditory system development: primary auditory neurons and their targets. *Annu. Rev. Neurosci.* 25, 51–101.

Rubel, E. W., Smith, D. J. and Miller, L. C. (1976). Organization and development of brain stem auditory nuclei of the chicken: ontogeny of n. magnocellularis and n. laminaris. *J. Comp. Neurol.* 166, 469–489.

Ruby, K., Falvey, K. and Kulesza, R. J. (2015). Abnormal neuronal morphology and neurochemistry in the auditory brainstem of Fmr1 knockout rats. *Neuroscience* 303, 285–298.

Sakuma, T., Nishikawa, A., Kume, S., Chayama, K. and Yamamoto, T. (2014). Multiplex genome engineering in human cells using all-in-one CRISPR/Cas9 vector system. *Sci Rep* 4,.

Scharkowski, F., Frotscher, M., Lutz, D., Korte, M. and Michaelsen-Preusse, K. (2018). Altered Connectivity and Synapse Maturation of the Hippocampal Mossy Fiber Pathway in a Mouse Model of the Fragile X Syndrome. *Cereb. Cortex* 28, 852–867.

Schecterson, L. C., Sanchez, J. T., Rubel, E. W. and Bothwell, M. (2012). TrkB downregulation is required for dendrite retraction in developing neurons of chicken nucleus magnocellularis. *J. Neurosci.* 32, 14000–14009.

Sears, J. C. and Broadie, K. (2018). Fragile X Mental Retardation Protein Regulates Activity-Dependent Membrane Trafficking and Trans-Synaptic Signaling Mediating Synaptic Remodeling. *Front. Mol. Neurosci.* 10, 440.

Seidl, A. H., Rubel, E. W. and Barría, A. (2014). Differential Conduction Velocity Regulation in Ipsilateral and Contralateral Collaterals Innervating Brainstem Coincidence Detector Neurons. *J. Neurosci.* 34, 4914–4919.

Serafini, T., Colamarino, S. A., Leonardo, E. D., Wang, H., Beddington, R., Skarnes, W. C. and Tessier-Lavigne, M. (1996). Netrin-1 Is Required for Commissural Axon Guidance in the Developing Vertebrate Nervous System. *Cell* 87, 1001–1014.

Shamay-Ramot, A., Khermesh, K., Porath, H. T., Barak, M., Pinto, Y., Wachtel, C., Zilberberg, A., Lerer-Goldshtein, T., Efroni, S., Levanon, E. Y., et al. (2015). Fmrp Interacts with Adar and Regulates RNA Editing, Synaptic Density and Locomotor Activity in Zebrafish. *PLOS Genetics* 11, e1005702.

Shepard, K. A., Korsak, L. I. T., DeBartolo, D. and Akins, M. R. (2020). Axonal localization of the fragile X family of RNA binding proteins is conserved across mammals. *J. Comp. Neurol.* 528, 502–519.

Shim, S.-O., Cafferty, W. B. J., Schmidt, E. C., Kim, B. G., Fujisawa, H. and Strittmatter, S. M. (2012). PlexinA2 limits recovery from corticospinal axotomy by mediating oligodendrocyte-derived Sema6A growth inhibition. *Mol. Cell. Neurosci.* 50, 193–200.

Šmít, D., Fouquet, C., Pincet, F., Zapotocky, M. and Trembleau, A. (2017). Axon tension regulates fasciculation/defasciculation through the control of axon shaft zippering. *eLife* 6, e19907.

Stoeckli, E. T. (2018). Understanding axon guidance: are we nearly there yet? *Development* 145, dev151415.

Strumbos, J. G., Brown, M. R., Kronengold, J., Polley, D. B. and Kaczmarek, L. K. (2010). Fragile X Mental Retardation Protein Is Required for Rapid Experience-Dependent Regulation of the Potassium Channel Kv3.1b. *Journal of Neuroscience* 30, 10263–10271.

Tessier, C. R. and Broadie, K. (2008). Drosophila fragile X mental retardation protein developmentally regulates activity-dependent axon pruning. *Development* 135, 1547–1557.

Varadarajan, S. G., Kong, J. H., Phan, K. D., Kao, T.-J., Panaitof, S. C., Cardin, J., Eltzschig, H., Kania, A., Novitch, B. G. and Butler, S. J. (2017). Netrin1 Produced by Neural Progenitors, Not Floor Plate Cells, Is Required for Axon Guidance in the Spinal Cord. *Neuron* 94, 790-799.e3.

Vonderschen, K. and Wagner, H. (2014). Detecting interaural time differences and remodeling their representation. *Trends in Neurosciences* 37, 289–300.

Wang, Z. and Storm, D. R. (2006). Extraction of DNA from mouse tails. *BioTechniques* 41, 410, 412.

Wang, Y. and Rubel, E. W. (2012). In Vivo Reversible Regulation of Dendritic Patterning by Afferent Input in Bipolar Auditory Neurons. *Journal of Neuroscience* 32, 11495–11504.

Wang, W., Bradley, A. and Huang, Y. (2009). A piggyBac transposon-based genome-wide library of insertionally mutated Blm-deficient murine ES cells. *Genome Research* 19, 667–673.

Wang, J., Miller, E. D., Simmons, G. S., Miller, T. A., Tabashnik, B. E. and Park, Y. (2010). piggyBac-like elements in the pink bollworm, Pectinophora gossypiella. *Insect Mol. Biol.* 19, 177–184.

Wang, Y., Sakano, H., Beebe, K., Brown, M. R., de Laat, R., Bothwell, M., Kulesza, R. J. and Rubel, E. W. (2014). Intense and specialized dendritic localization of the fragile X mental retardation protein in binaural brainstem neurons: a comparative study in the alligator, chicken, gerbil, and human. *J. Comp. Neurol.* 522, 2107–2128.

Wang, T., de Kok, L., Willemsen, R., Elgersma, Y. and Borst, J. G. G. (2015a). In vivo synaptic transmission and morphology in mouse models of Tuberous sclerosis, Fragile X syndrome, Neurofibromatosis type 1, and Costello syndrome. *Front. Cell. Neurosci.* 9,.

Wang, B., Pan, L., Wei, M., Wang, Q., Liu, W.-W., Wang, N., Jiang, X.-Y., Zhang, X. and Bao, L. (2015b). FMRP-Mediated Axonal Delivery of miR-181d Regulates Axon Elongation by Locally Targeting Map1b and Calm1. *Cell Reports* 13, 2794–2807.

Wang, X., Zorio, D. A. R., Schecterson, L., Lu, Y. and Wang, Y. (2018). Postsynaptic FMRP Regulates Synaptogenesis In Vivo in the Developing Cochlear Nucleus. *J. Neurosci.* 38, 6445–6460.

Wang, X., Hong, H., Brown, D. H., Sanchez, J. T. and Wang, Y. (2017). Distinct Neural Properties in the Low-Frequency Region of the Chicken Cochlear Nucleus Magnocellularis. *eNeuro* 4,.

Wang, X., Zorio, D. A. R., Schecterson, L., Lu, Y. and Wang, Y. (2018). Postsynaptic FMRP Regulates Synaptogenesis In Vivo in the Developing Cochlear Nucleus. *J. Neurosci.* 38, 6445–6460.

Weisinger, K., Kohl, A., Kayam, G., Monsonego-ornan, E. and Sela-donenfeld, D. (2012). Expression of hindbrain boundary markers is regulated by FGF3. *Biology Open* 1, 67–74.

Wurster, S., Kumaresan, P. R., Albert, N. D., Hauser, P. J., Lewis, R. E. and Kontoyiannis, D. P. (2019). Live Monitoring and Analysis of Fungal Growth, Viability, and Mycelial Morphology Using the IncuCyte NeuroTrack Processing Module. *mBio* 10, e00673-19, /mbio/10/3/mBio.00673-19.atom.

Xu, B., Zhang, Y., Zhan, S., Wang, X., Zhang, H., Meng, X. and Ge, W. (2018). Proteomic Profiling of Brain and Testis Reveals the Diverse Changes in Ribosomal Proteins in fmr1 Knockout Mice. *Neuroscience* 371, 469–483.

Xu, J., Berret, E. and Kim, J. H. (2017). Activity-dependent formation and location of voltage-gated sodium channel clusters at a CNS nerve terminal during postnatal development. *J. Neurophysiol.* 117, 582–593.

Young, S. R. and Rubel, E. W. (1986). Embryogenesis of arborization pattern and topography of individual axons in N. Laminaris of the chicken brain stem. *J. Comp. Neurol.* 254, 425–459.

Yu, X., Wang, X., Sakano, H., Zorio, D. A. R. and Wang, Y. (2020). Dynamics of the Fragile X Mental Retardation Protein Correlates with Cellular and Synaptic Properties in Primary Auditory Neurons following Afferent Deprivation. *Journal of Comparative Neurology.* doi: 10.1002/cne.24959. Online ahead of print.

Yung, A. R., Druckenbrod, N. R., Cloutier, J.-F., Wu, Z., Tessier-Lavigne, M. and Goodrich, L. V. (2018). Netrin-1 Confines Rhombic Lip-Derived Neurons to the CNS. *Cell Reports* 22, 1666–1680.

Zimmer, S. E., Doll, S. G., Garcia, A. D. R. and Akins, M. R. (2017). Splice form-dependent regulation of axonal arbor complexity by FMRP. *Dev Neurobiol* 77, 738–752.

Zorio, D. A. R., Jackson, C. M., Liu, Y., Rubel, E. W. and Wang, Y. (2017). Cellular distribution of the fragile X mental retardation protein in the mouse brain. *J. Comp. Neurol.* 525, 818–849.

	Exon of *Fmr1*	
G3	Exon8	GAGGTGGACCAACTACGTT
G4	Exon8	ACGTGGTCCAGGCTACGCTT
control		GGGTCTTCGAGAAGACCTG
Test-F3	Exon8	AGGTTGCTACCAGCTGTTGG
Test-F4	Exon8	TACTGCTATGAATAGCTCCTG
Test-R1	Exon8	GAAGCTATGTGCAAATATTAGCAG
Test-R2	Exon8	TTCTCATTGAACACTTGCATTTCC

Table 1. Plasmid sequences for gRNA production and validation.

Figures

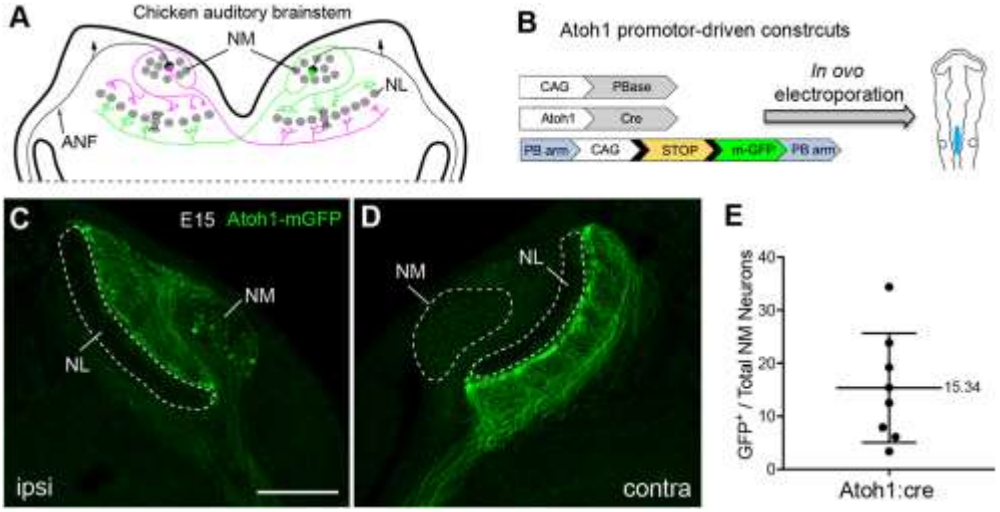

Figure 1. High-specificity genetic labeling of NM precursors and neurons. A. Schematic drawing of the NM-NL circuit. **B.** Plasmid design for Atoh1-mGFP. Electroporation is performed following plasmid injection into rhombomeres 5-6 (r5-6; dark blue). **C.** E15 brainstem sections showing a restricted localization of $mGFP^+$ cell bodies in NM on the transfection (ipsi) side. Yellow stars indicate bilateral NM axons to NL. **E.** Ratio of transfected neurons in NM. The mean value is indicated for this and all plots in subsequent figures. Abbreviations: ANF, auditory nerve fiber; ipsi, ipsilateral; contra, contralateral. Scale bar: 200 µm in C.

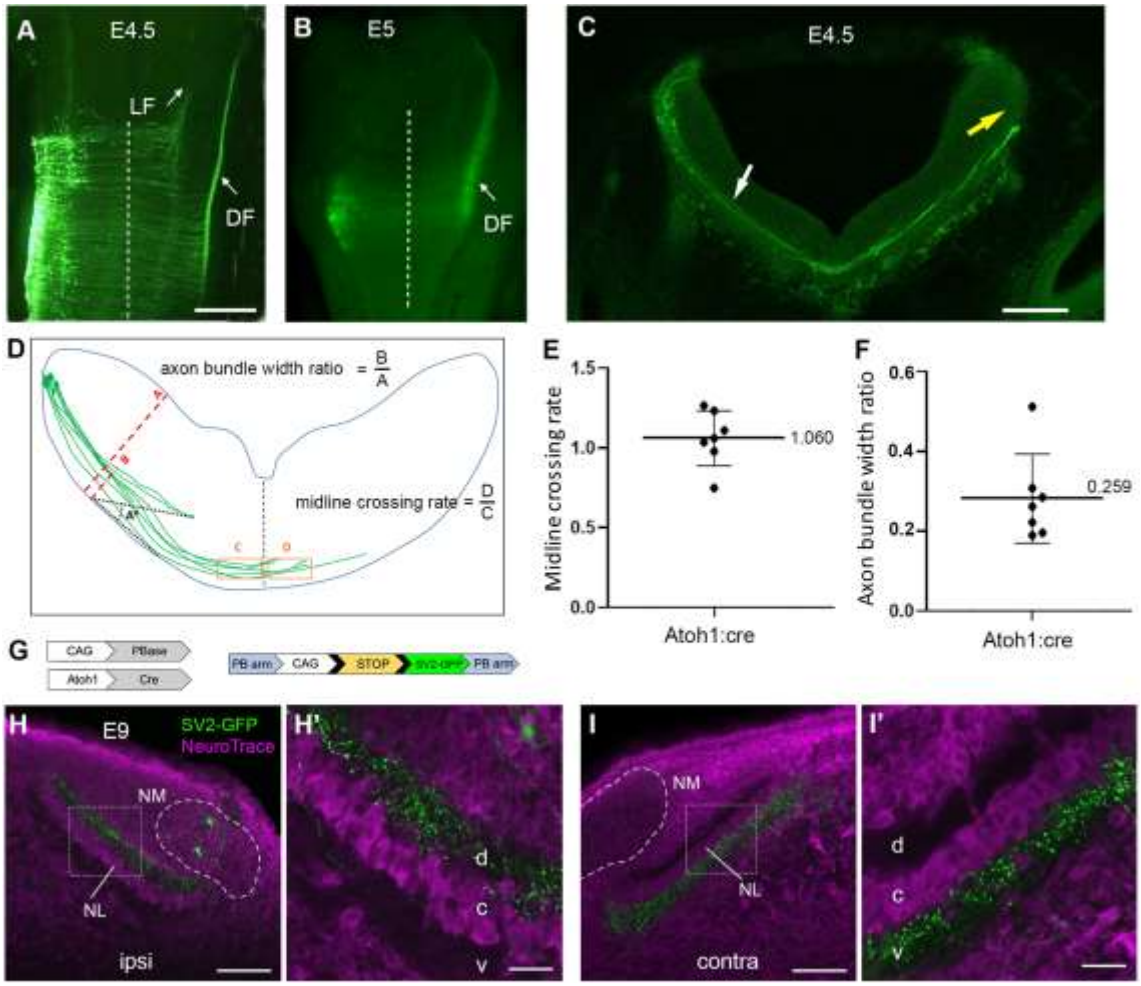

Figure 2. Axon development of NM precursors and neurons. Images were taken from embryos electroporated with Atoh1-mGFP at E2-2.5. **A.** Flat-mount view at E4.5 showing two contralateral projection bundles (LF and DF) of Atoh1/dA1 cells. **B.** Top view at E5 showing that axons of Atoh1/dA1 cells at r5-6 join the DF bundle. Dashed lines indicate the midline. **C.** Transverse section at E4 at the level of r5-6. $mGFP^+$ axons have crossed the midline and arrived in their contralateral target area (yellow arrow). **D.** An illustration describing the measurements used to quantify axonal growth patterns of NM precursors. Axon bundle width was calculated as the ratio between B (GFP^+ fascicule width) divided by A (mantle-ventricular width). Axonal midline crossing rate was calculated as D (area of GFP^+ contralateral axons) divided by C (area of GFP^+ ipsilateral axons). A^o was the angle between the most medial GFP+ projecting axon and the mantle plate. **E-F.** Box plot analysis of the ratio of axonal midline crossing (E) and bundle width (F) of Atoh1:cre tagged axons at E4.5. Each data point represents one embryo (n=7). **G.** Plasmid design for SV2-GFP with Atoh1-enhancer and PiggyBac (PB) transposase. **H-I'.** SV2-GFP

(green) distribution in transverse sections counterstained with NeuroTrace (magenta) on the ipsilateral (H-H') and contralateral (I-I') sides. H' and I' are enlarged views of the boxes in H and I, respectively. NM is outlined by dashed circles. The cell body layer (c) as well as the dorsal (d) and ventral (v) dendrite domains of the NL are indicated. Abbreviations: LF, lateral funiculus; DF, dorsal funiculus. Scale bars: 1 mm in A (applies to A-B) and C; 100 μm in H and I; 20 μm in H' and I'.

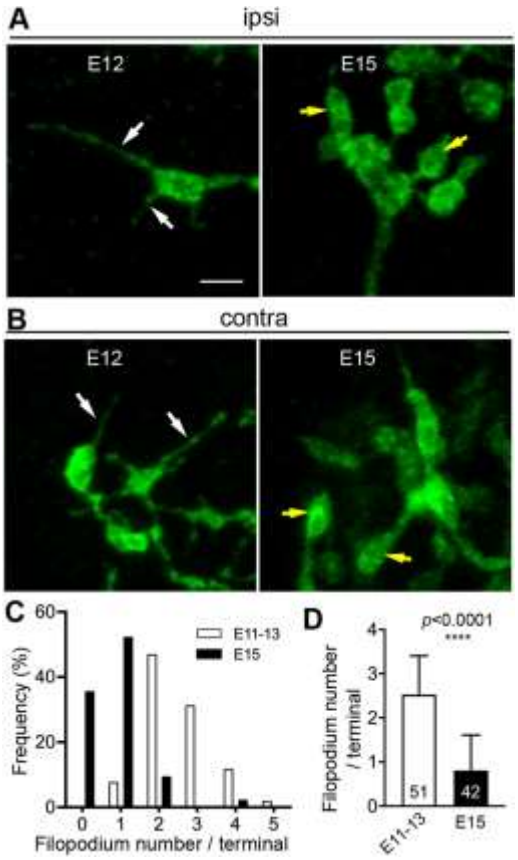

Figure 3: Morphological maturation of presynaptic terminals of NM neurons. Images were taken from embryos electroporated with Atoh1-mGFP at E2. **A-B.** NM axon terminals in the dorsal neuropil of the ipsilateral NL (A) and in the ventral neuropil of the contralateral NL (B) at E12 and E15. NM axons show a growth cone structure with filopodia (white arrows) at E12 and bouton-like terminals (yellow arrows) at E15. **C-D.** Frequency distribution (B) and population analysis (C) of the number of filopodia per terminal at E11-13 (n=51 terminals) and E15 (n=42 terminals). Additional images and data analyses are shown in Figs. S3,S4. Scale bars: 2 µm.

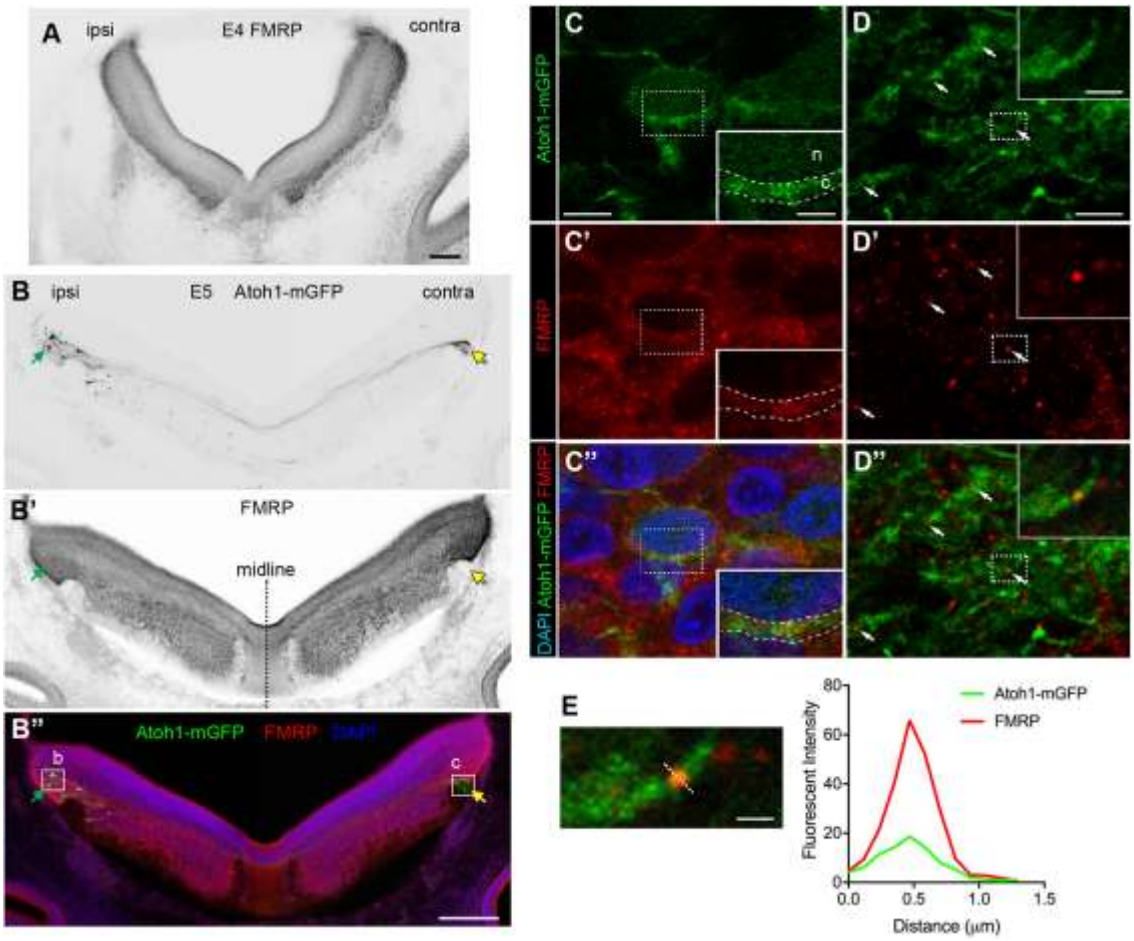

Figure 4. Endogenous FMRP is localized in distal axons of NM precursors. A. FMRP immunostaining taken from an E4 embryo**. B-B''.** FMRP immunostaining (B') taken from an E5 embryo transfected with Atoh1-mGFP (B)**.** B'' is the merged image. Note the FMRP immunostaining in the region where transfected cell bodies are located (green arrows). The terminal region on the contralateral side (yellow arrows) is low in FMRP immunoreactivity. **C-C''.** High-magnification images of the box in B'' from the transfection (ipsi) side. Transfected cells (green) contain FMRP immunoreactivity (red) in the cytoplasm (c in insets) and a weaker staining in the nuclear (n in insets). **D-D''.** High-magnification images of the box in B'' from the contralateral side (contra). A subset of FMRP puncta are localized in mGFP^{+} axon processes (insets). FMRP puncta that are localized beyond mGFP^{+} axon processes are presumably in untransfected axons because this region contains no cell bodies as indicated with the lack of DAPI-labeled nuclei. **E.** Colocalization analysis of a representative FMRP punctum with Atoh1-mGFP^{+} labeled axon, confirming the axonal location of FMRP. Scale bars:100 μm in A; 200 μm in B'' (applies to B-B''); 5 μm in C and D (applies to C-D''); 2 μm for insets; 1 μm in E.

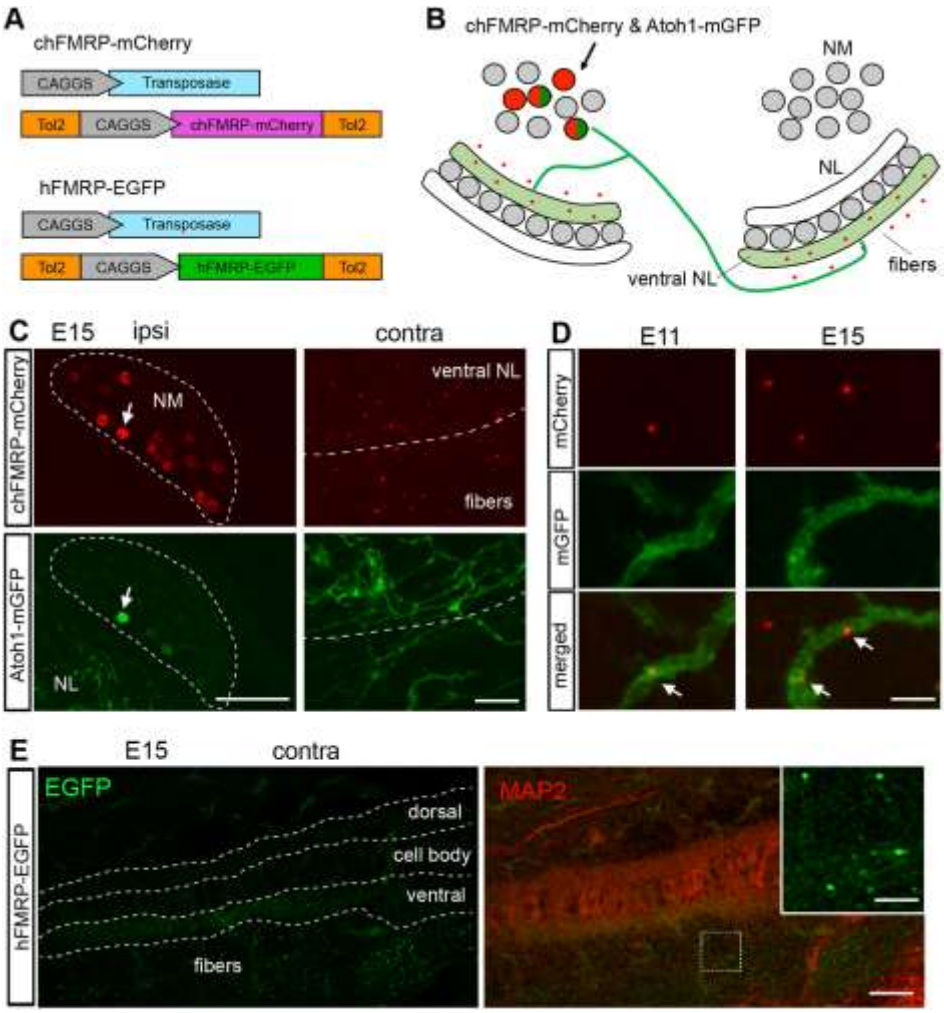

Figure 5. Axon localization of FMRP in NM neurons. A. Plasmid designs for constitutive expression of chicken and human FMRP (chFMRP and hFMRP). **B.** Schematic drawing of the co-transfection protocol for chFMRP-mCherry and Atoh1-mGFP. **C.** Transverse sections at E15 showing transfected cell bodies in NM (left column) and their contralateral projection in NL (right column), following the co-transfection shown in B. White arrow indicates a co-transfected NM neuron. On the contralateral side, chFMRP-mCherry puncta are detected within the ventral neuropil domain of NL as well as the fiber region containing incoming NM axons. **D.** High magnification images of the ventral neuropil of the contralateral NL at E11 and E15. A subset of FMRP-mCherry puncta are located in Atoh1-mGFP+ NM axons (arrows). **E.** Images of the contralateral NL at E15 following transfection with hFMRP-EGFP and MAP2 counterstaining (red), a somatodendritic marker. hFMRP puncta are distributed in the ventral fiber region and the ventral NL neuropil. Abbreviation: MAP2, microtubule-associated protein 2. Scale bars: 100 µm in the left column of C; 20 µm in the right column of C; 5 µm in D; 50 µm in E; 7.5 µm in inset.

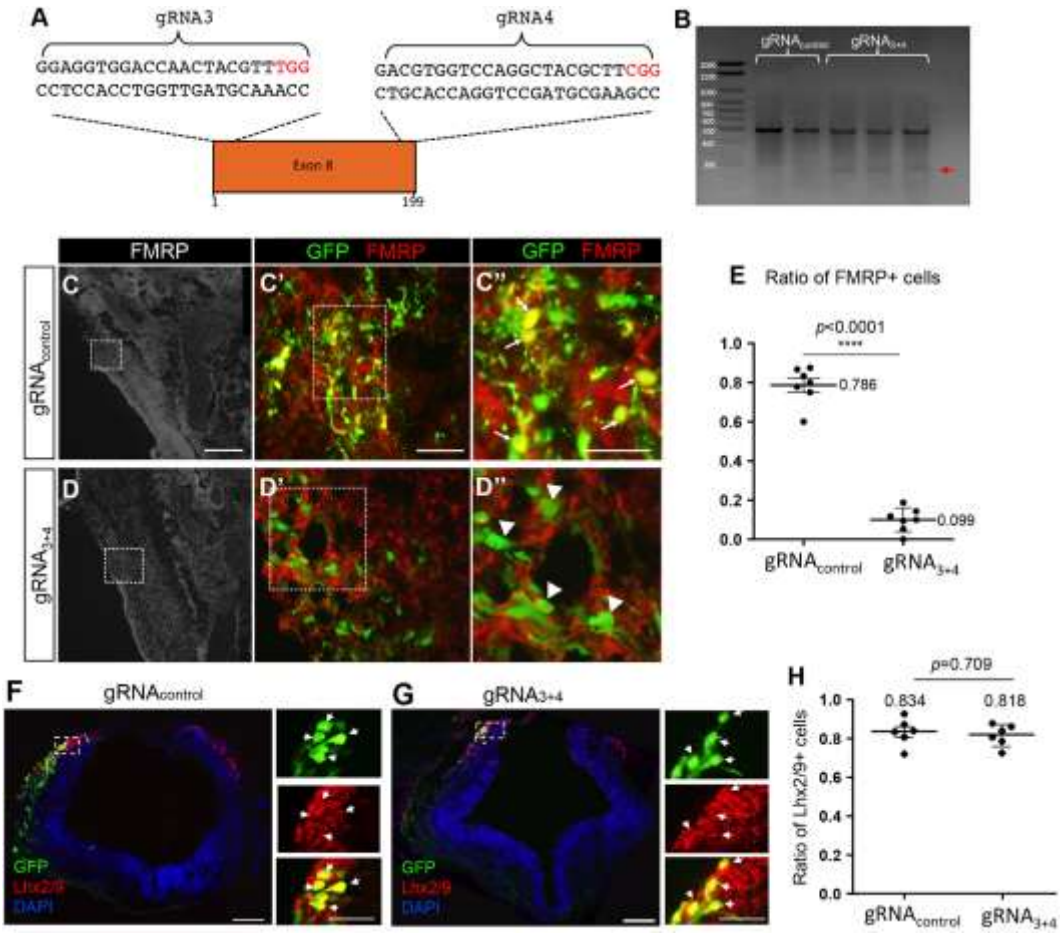

Figure 6. FMRP knockout with Crispr/Cas9 strategy. A. Crispr design of FMRP sequence in exon 8. **B.** Gel electrophoresis of PCR products from hindbrains electroporated with $gRNA_{control}$ and $gRNA_{3+4}$ plasmids. Red arrow points to a ~260 bp fragment obtained by Cas9 deletion. **C-D.** Sagittal-section views of E6.5 brainstems expressing $gRNA_{control}$ (C) or $gRNA_{3+4}$ (D) plasmids (green) and stained for FMRP antibody (red). High-magnification views of the boxed areas in C-D and C'-D' appear in the right panel of each image. Arrows and arrowheads point to $FMRP^+$ and $FMRP^-$ cells, respectively. **E.** Box plot quantification of FMRP-immunoreactive cells out of total GFP^+ cells. Each data point represents one embryo (n=7 embryos for each group). **F-G.** Cross-section views of E4.5 hindbrains obtained from embryos that were electroporated with $gRNA_{control}$ or $gRNA_{3+4}$ (F-G, green) and stained with Lhx2/9 antibody (red). Higher-magnification views of the boxed areas in F and G are represented in the right of each panel in different channels. Arrows indicate the same cells in all channels. H. Box plot quantification of Lhx2/9 immunoreactive cells out of total GFP^+ cells. Each data point represents one section (n=3 embryos for each group). Scale bars: 100 μm in C (applies to C-D) and G (applies to F-G); 50 μm in C' (applies to C'-D'); 20 μm in C'' (applies to C''-D''); 50 μm in insets in F, G.

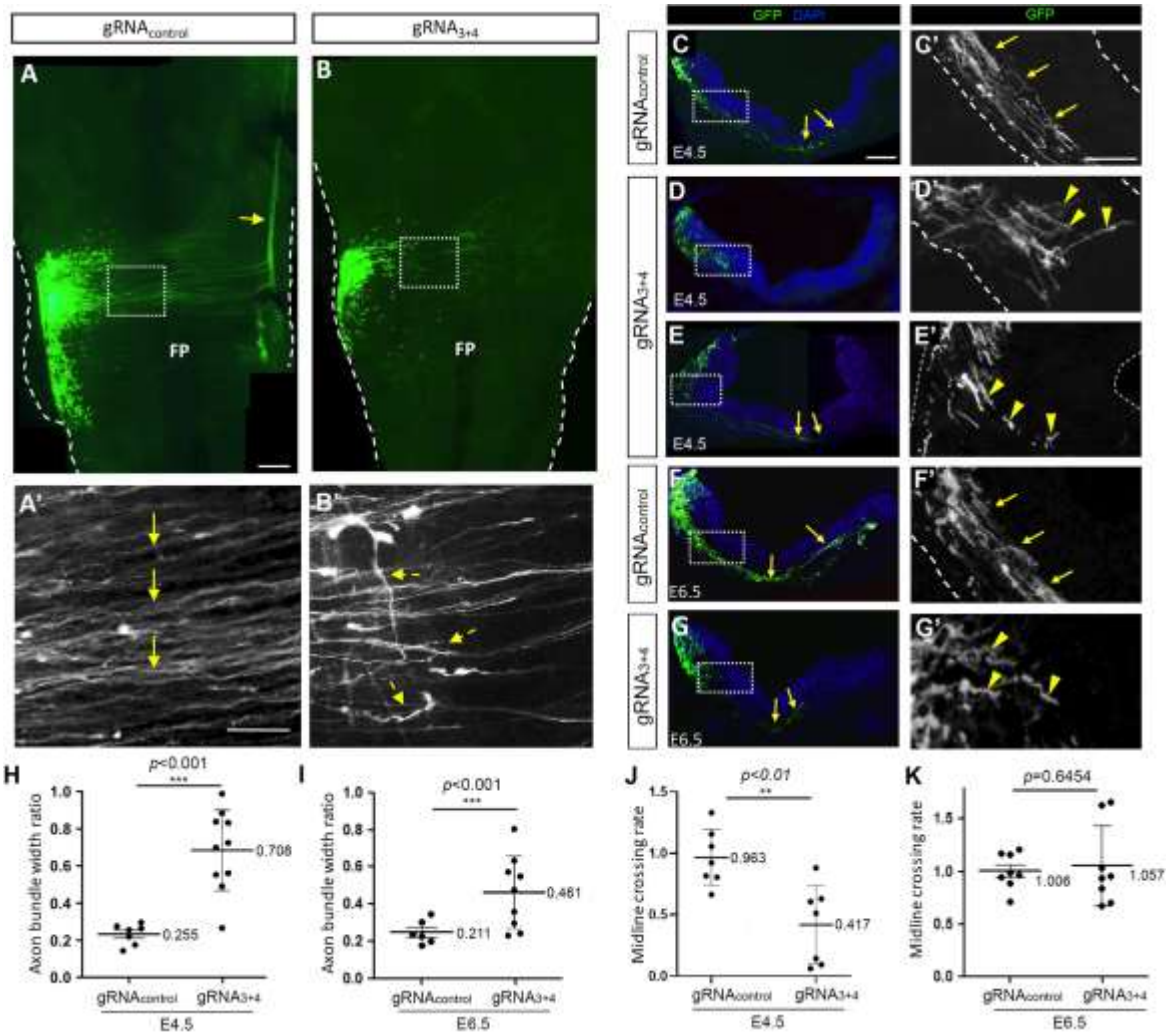

Figure 7. Crispr-mediated FMRP knockout induces disoriented axonal growth. A-B. E4.5 flat-mounted hindbrains from embryos electroporated at E2.5 with $gRNA_{control}$ (A) or $gRNA_{3+4}$ (B). Higher-magnification views of the boxed areas in A, B are represented at A', B'. Arrows point to organized axons in A. Dashed arrows in B' indicate disoriented axons. **C-G'.** Transverse sections of r5-6 level at E4.5 (C-E') and E6.5 (F-G') from embryos electroporated with $gRNA_{control}$ (C-C', F-F') or $gRNA_{3+4}$ (D-E', G-G') plasmids. Higher-magnification views of the boxed areas in the left panels (C-G) are represented in the right panels (C'-G'). Arrows in the left panels indicate axons that crossed the midline. Arrows and arrowheads in the right panels point to organized and disorganized axons, respectively. **H-I.** Box plot analysis of the width of the GFP^+ axonal bundle at E4.5 (H) and E6.5 (I). **J-K.** Box plot analysis of the axonal midline crossing rate at E4.5 (J) and E6.5 (K). Each data point represents one embryo. Abbreviation: FP, floor plate. Scale bars = 100 µm in A (applies to A, B); 50 µm in A' (applies to A', B'); 100 µm in C (applies to C, D, E, F, G); 50 µm in C' (applies to C', D', E', F', G').

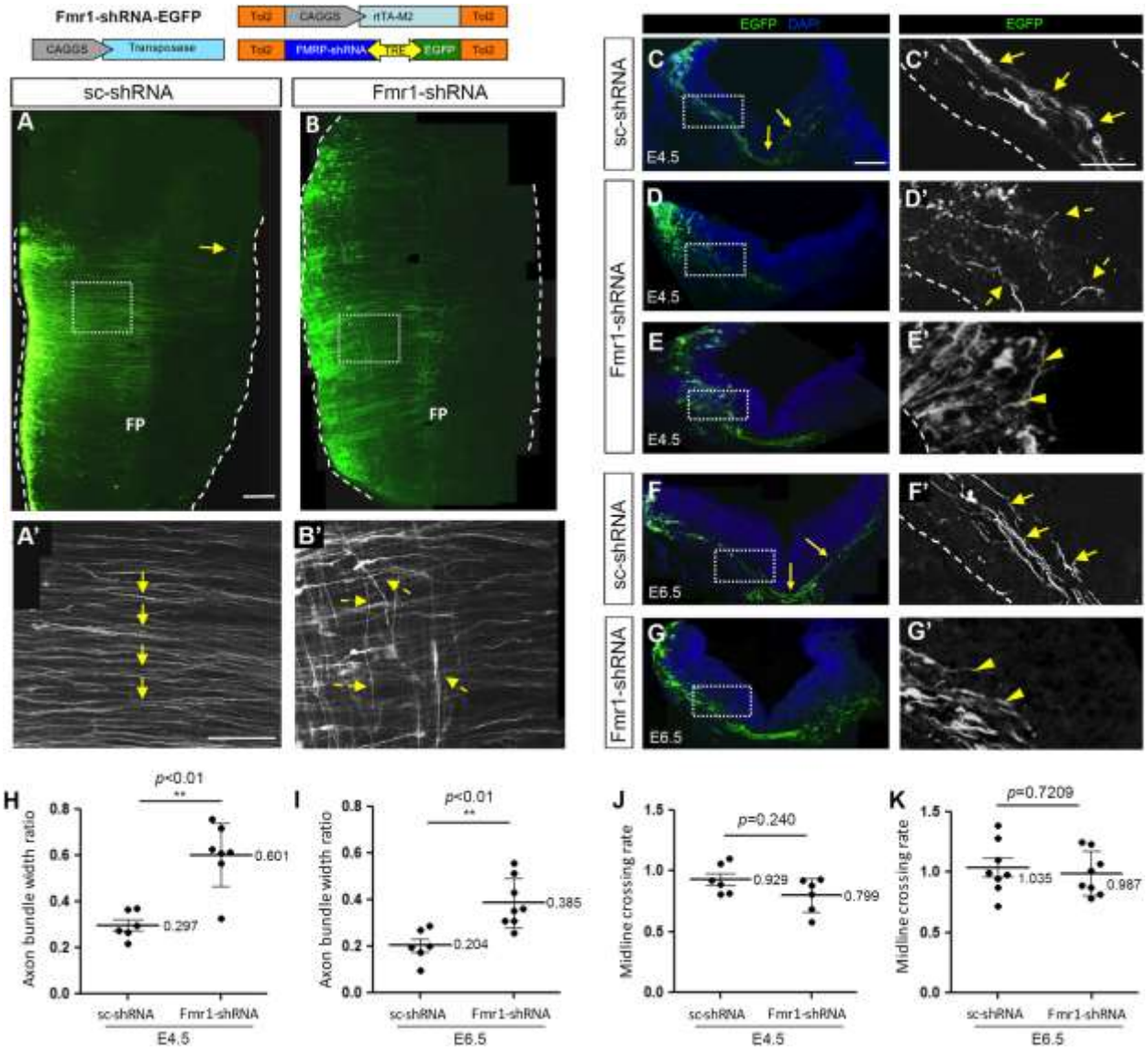

Figure 8. shRNA-mediated FMRP knockdown induces axonal disorganization. A-B. E4.5 flat-mounted hindbrains from embryos that were electroporated at E2.5 with scrambled-shRNA-EGFP (sc-shRNA; A) or *Fmr1*-shRNA-EGFP (B). Higher-magnification views of the boxed areas in A, B are represented at A', B'. Plasmid design for *Fmr1*-shRNA is illustrated on the top. Arrows and dashed arrows represent organized and disoriented axons, respectively. **C-G'.** Transverse sections of r5-r6 level at E4.5 (C-E') and E6.5 (F-G') from embryos electroporated with sc-shRNA (C-C', F-F') or *Fmr1*-shRNA (D-E', G-G') plasmids. Higher-magnification views of the boxed areas in the left panels (C-G) are represented in the right panels (C'-G'). Arrows in left panels indicate axons that crossed the midline. Arrows and arrowheads in the right panels point to organized and disorganized axons, respectively. **H-I.** Box plot analysis of the width of the GFP^+ axonal bundle at E4.5 (H) and E6.5 (I). **J-K.** Box plot analysis of the axonal midline crossing rate at E4.5 (J) and

E6.5 (K). Each data point presents one embryo. Abbreviation: FP, floor plate. Scale bars: 100 μm in A (applies to A, B); 50 μm in A’ (applies to A’, B’); 100 μm in C (applies to C, D, E, F, G); 50 μm in C’ (applies to C’, D’, E’, F’, G’).

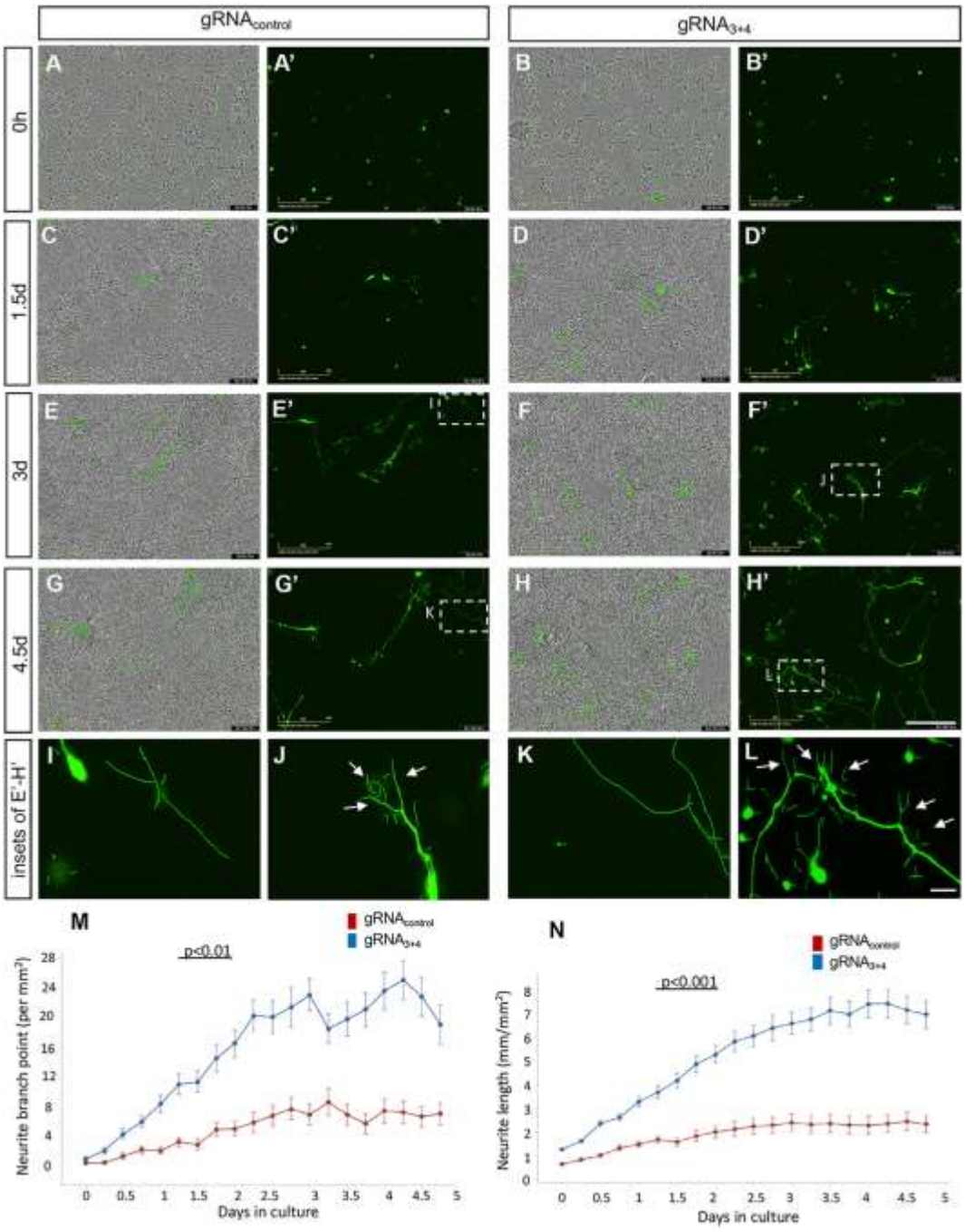

Figure 9. Crispr-mediated FMRP knockout induces neurite overgrowth and overbranching in hindbrain culture. A-H'. Time-lapse analysis of cell cultures obtained from E3.5 hindbrains that were electroporated at E2.5 with $gRNA_{control}$ (A, C, E, G) and $gRNA_{3+4}$ (B, D, F, H) plasmids. Cells were documented every 6 hours for 5 days. Representative phase and green fluorescence images in different time points are shown. GFP^+ neurites are evident in all images. **I-L.** Higher-magnification views of the boxed areas in above panels (E-H) are represented in the bottom

panels, respectively. Arrows in panels (K, L) show overbranching along the neurite up to its terminal. **M-N.** Quantification of neurite branch point (M) and neurite length (N) along 5 days using NeuroTrack analysis. Each data point represents 6 different wells of a 48-well plate. Scale bars: 200 μm in H' (applies to A-H'); 50 μm in L (applies to I-L).

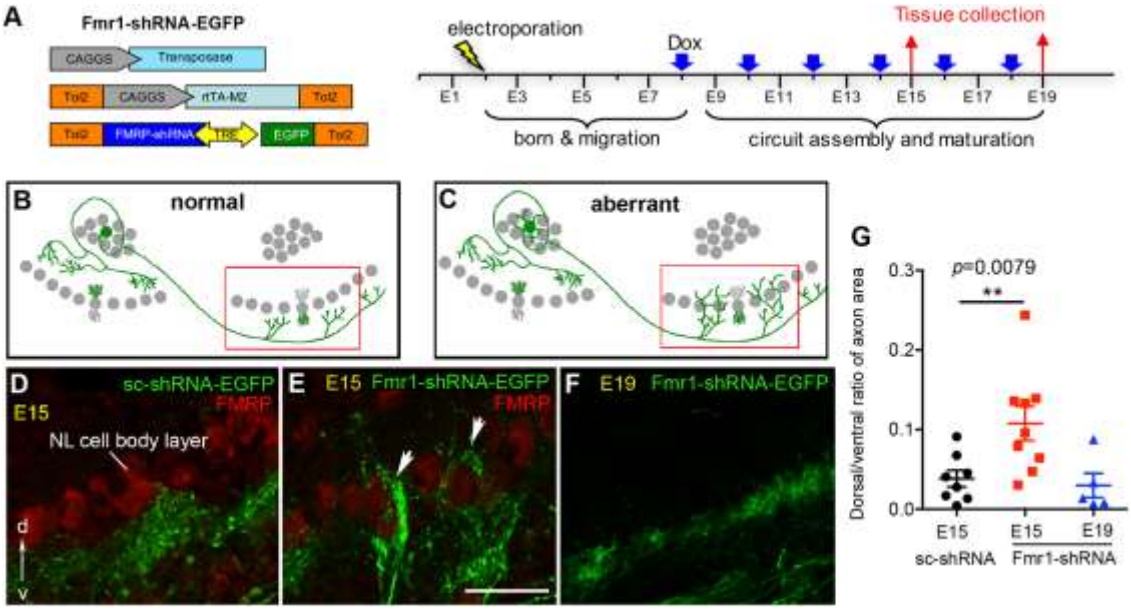

Figure 10. FMRP knockdown leads to axon projection errors in NL. A. Transfection protocol for late-onset shRNA expression. Blue arrows point out the days for Dox treatment. **B-C.** Schematic drawings of normal (B) and aberrant (C) axon targeting of NM neurons in the contralateral NL. **D-E.** Photomicrographs of NM axons in the contralateral NL at E15 following scrambled-shRNA (D) and *Fmr1*-shRNA (E) expression. Arrows point to abnormally projected NM axons through the cell body layer into the dorsal neuropil. **F.** NM axons in the contralateral NL at E19 following *Fmr1*-shRNA expression. The axons are predominantly distributed in the ventral neuropil, similar to the control. Dashed lines indicate the cell body layer. **G.** Quantification of the dorsal/ventral ratio of axon area. This ratio is significantly increased in *Fmr1*-shRNA transfected embryos at E15 (red squares) but not E19 (blue triangles), as compared to control embryos (black circles). Scale bars: 50 μm in D, E, F.

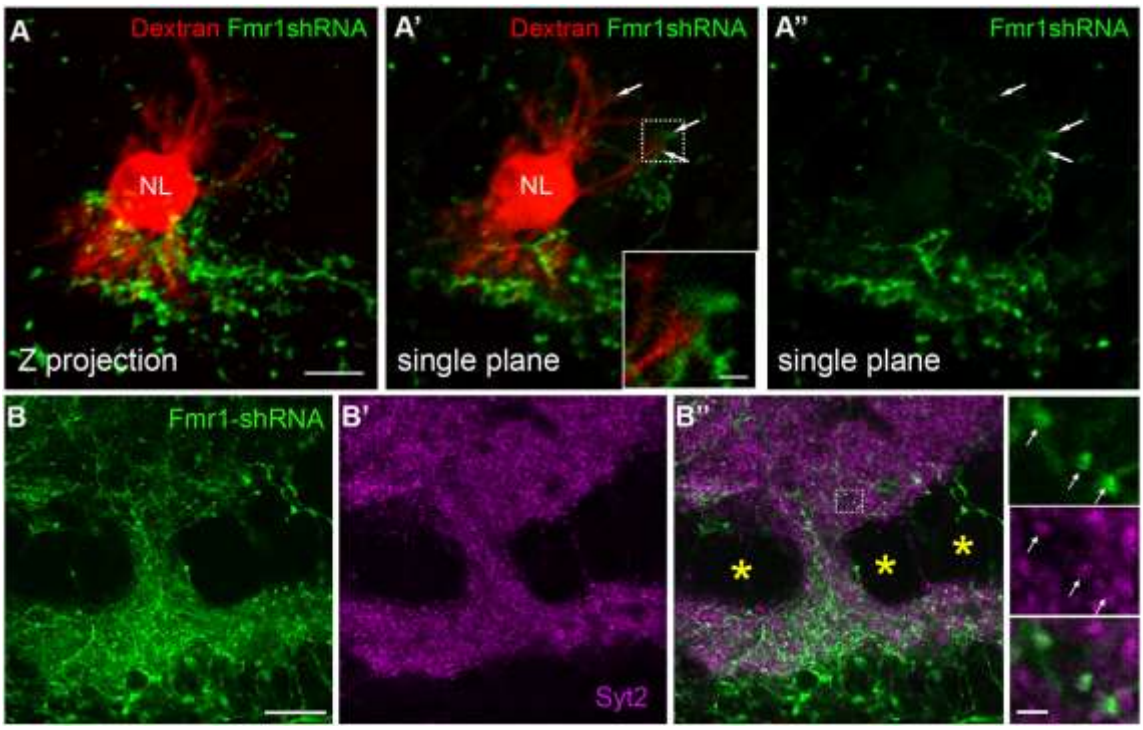

Figure 11. Aberrantly projected NM axons form synapses on NL dendrites. NM precursors were unilaterally transfected with *Fmr1*-shRNA-EGFP. Images were taken from the side contralateral to the transfection. **A-A''.** Images of a dye-filled NL neuron (red) whose dorsal and ventral dendrites are in close contact with EGFP$^+$ NM axons (white arrows). **B-B''.** Double labeling of Syt2 immunoreactivity with EGFP$^+$ NM axons. Stars indicate NL cell bodies in B''. Higher-magnification views of the boxed area in I'' are represented in the right panels. EGFP$^+$ axonal terminals (white arrows) are immunoreactive to Syt2. Scale bars: 10 μm in A, 2 μm in inset of A', 20 μm in B, and 2 μm in the right most column. Abbreviation: Syt 2, synaptotagmin 2.

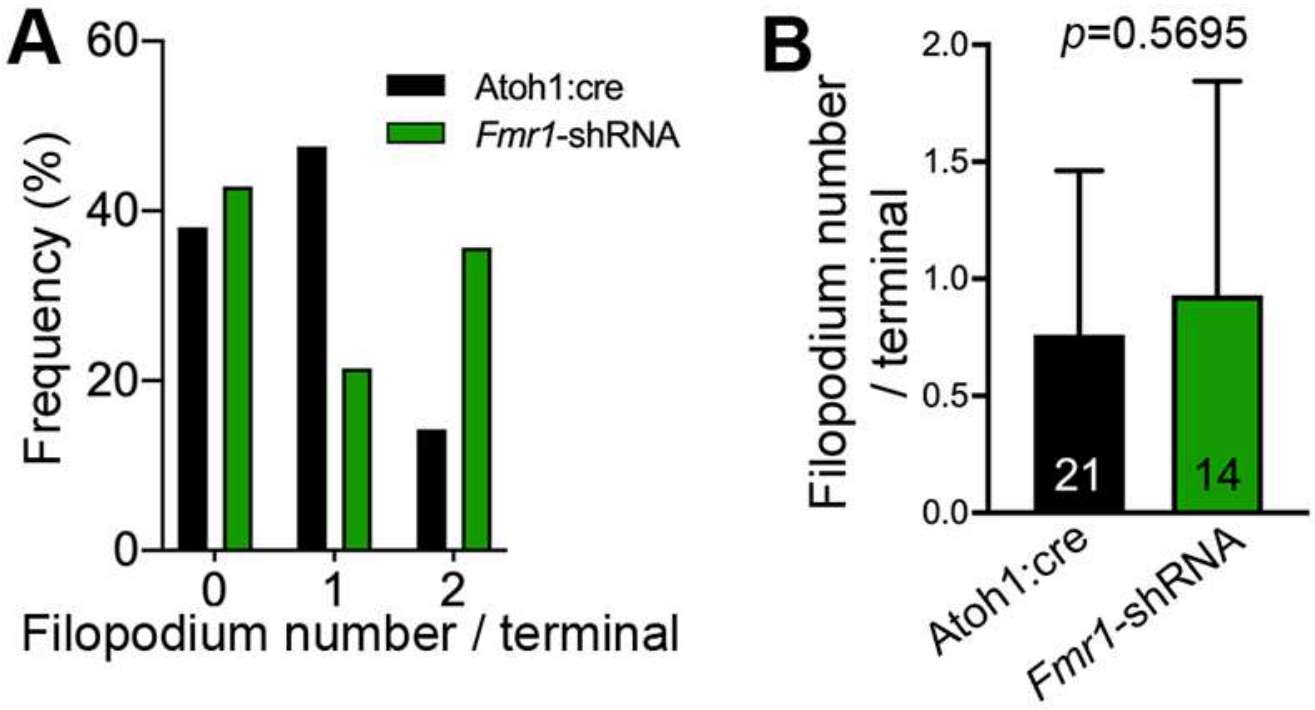

Figure 12. FMRP knockdown does not affect the morphological maturation of NM axonal terminals. A-B. Frequency distribution (A) and population analysis (B) of the number of filopodia per terminal following transfection with Atoh1:cre-mGFP (black bars; n=21 terminals) and *Fmr1*-shRNA (green bars; n=14 terminals). All terminals were measured form the ventral neuropil of the contralateral NL.

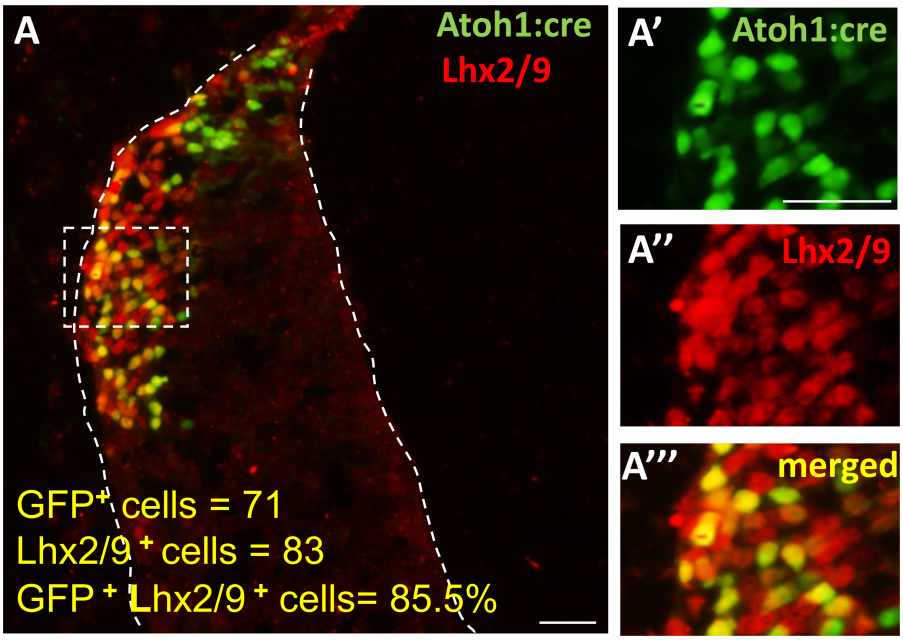

Figure S1. Atoh1:cre transfected cells are immunoreactive to Lhx2/9. Transverse section of E3.5 hindbrain (r5) that was electroplated at E2.5 with Atoh1:cre-nGFP plasmid and stained for Lhx2/9 to label endogenous dA1 cells. The dorsal half of the electroporated side of the neural tube is shown, demonstrating GFP^+ nuclei co-labeled with Lhx2/9 (n=7 embryos). Counting of cell nuclei expressing Atoh1:cre-GFP, Lhx2/9 or both in this section is provided in the lower left, demonstrating that 85.5% of electroporated cells co-express Lhx2/9. This ratio is in accordance with our previous publication (Kohl et al., 2012) that found 88% overlapping of Atoh1:cre with Lhx2/9 expressing cells. High-magnification views of the boxed area in (A) are represented in panels (A'-A''') in the different channels. Scale bars: 100um in A; 50um in A'.

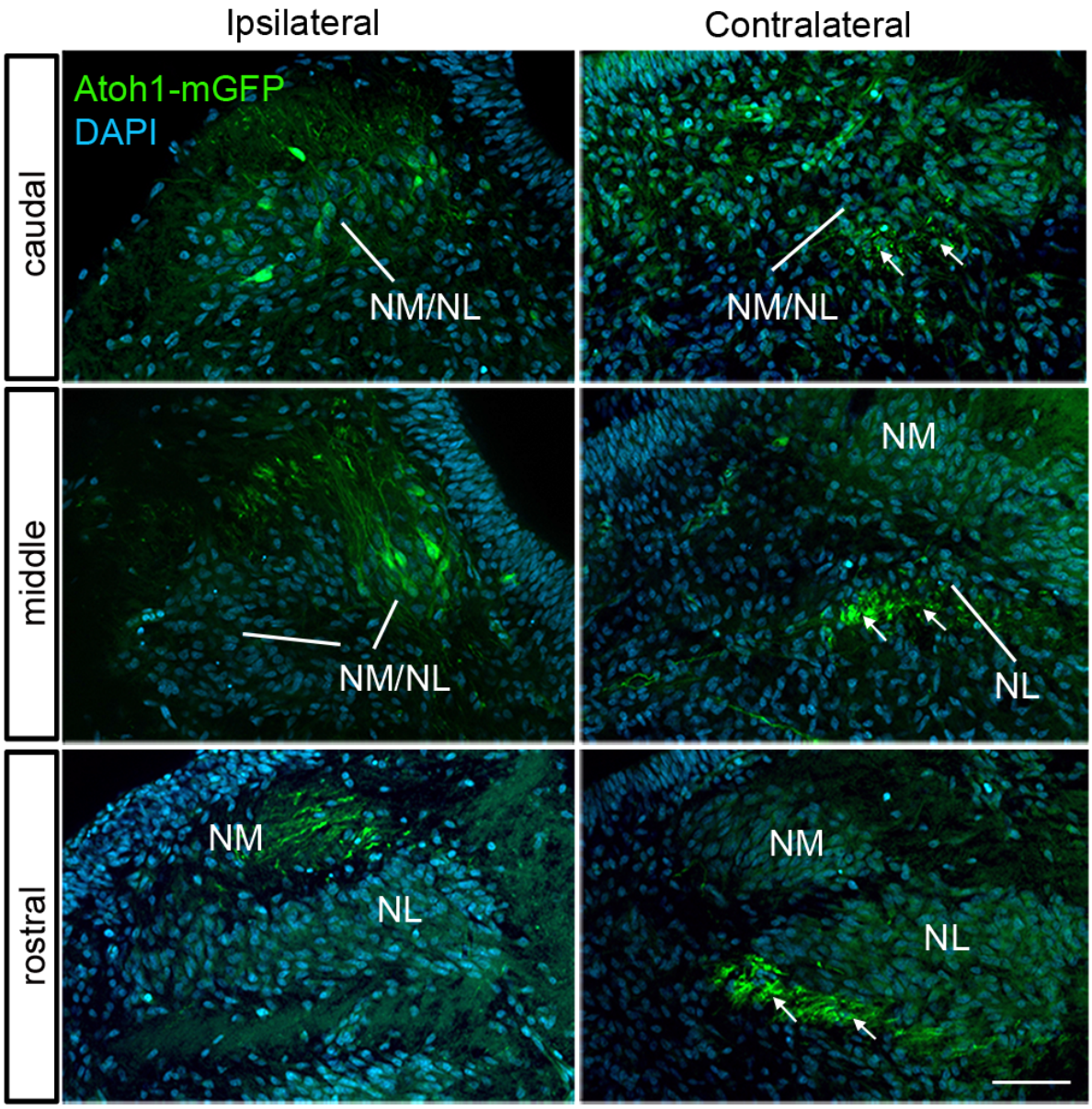

Figure S2. Separation of NM and NL at E7. Atoh1-mGFP labeling (green) at E7 on sections counterstained with DAPI (blue). At this stage, the NL and NM are migrating away from each other at the rostral level, while still merged at more caudal levels. White arrows point to the contralateral mGFP^{+} axons ventral to the NM/NL. Scale bars: 50 μm.

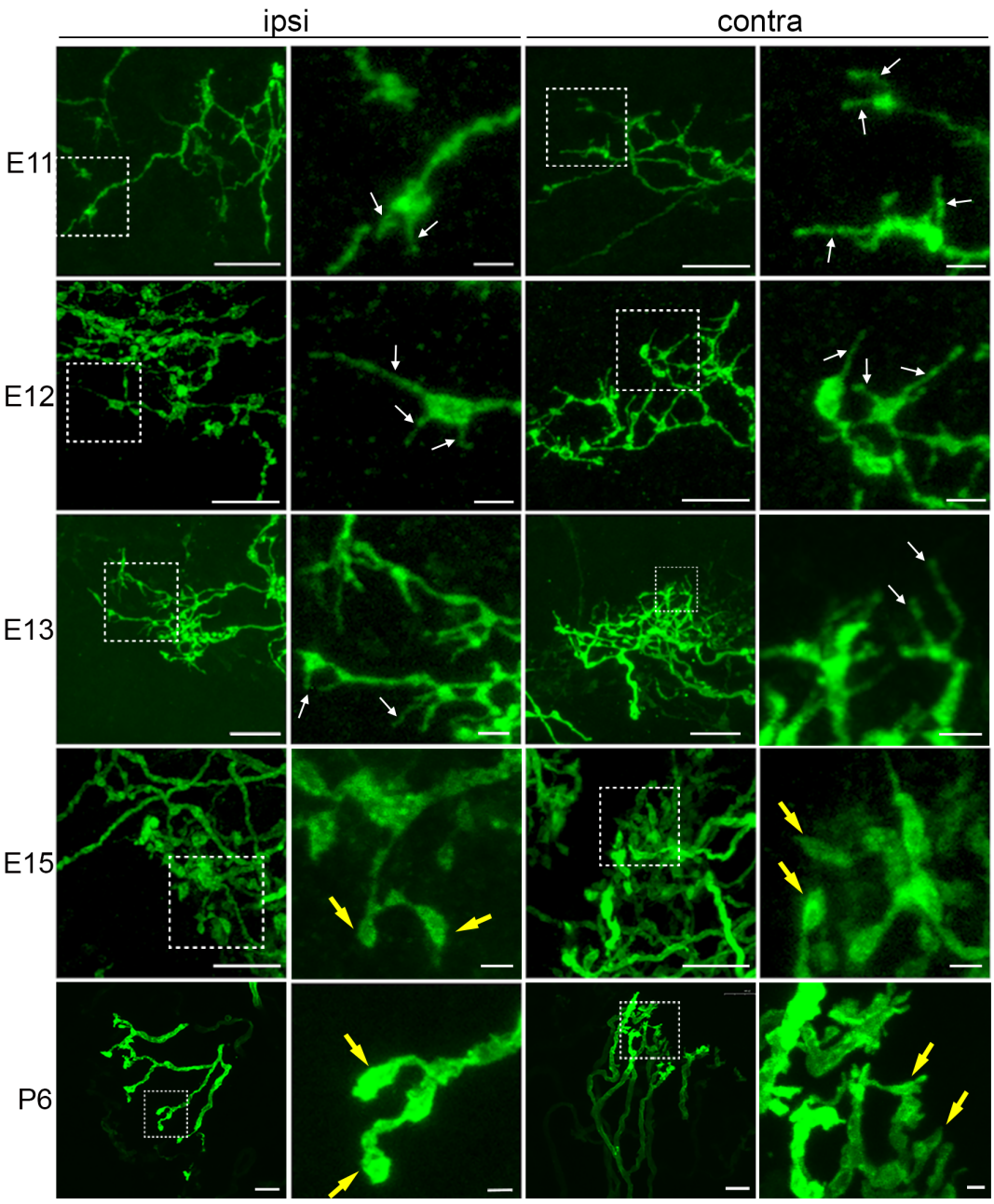

Figure S3. Morphological maturation of presynaptic terminals of NM neurons. Images were taken from embryos electroporated with Atoh1-mGFP at E2. The left two columns show NM axon terminals in the dorsal neuropil of the ipsilateral NL, while the right two columns show axons in the ventral neuropil of the contralateral NL. High-magnification views of the boxed areas appear in the right panel of each image. NM axons show a growth cone structure with filopodia (white arrows) at E11-13 and mature terminal morphology (yellow arrows) at E15 and later. Abbreviations: E, embryonic; P, post-hatch. Scale bars: 10 μm in lower-magnification images (columns 1, 3); 2 μm in higher-magnification images (columns 2, 4).

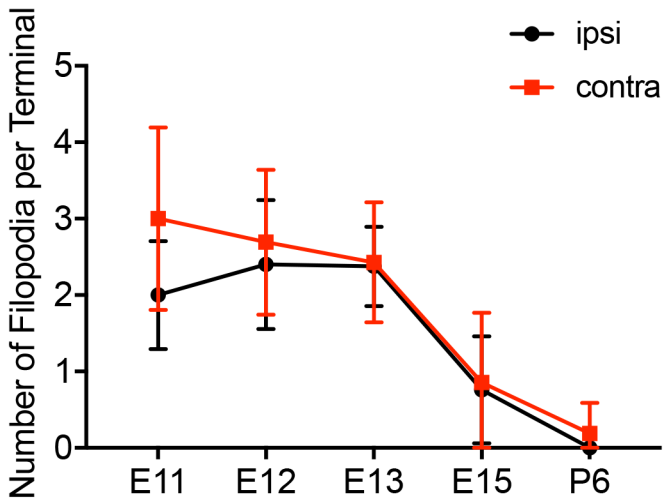

Figure S4. Quantification of terminal morphology at E11, E12, E13, E15 and P6.

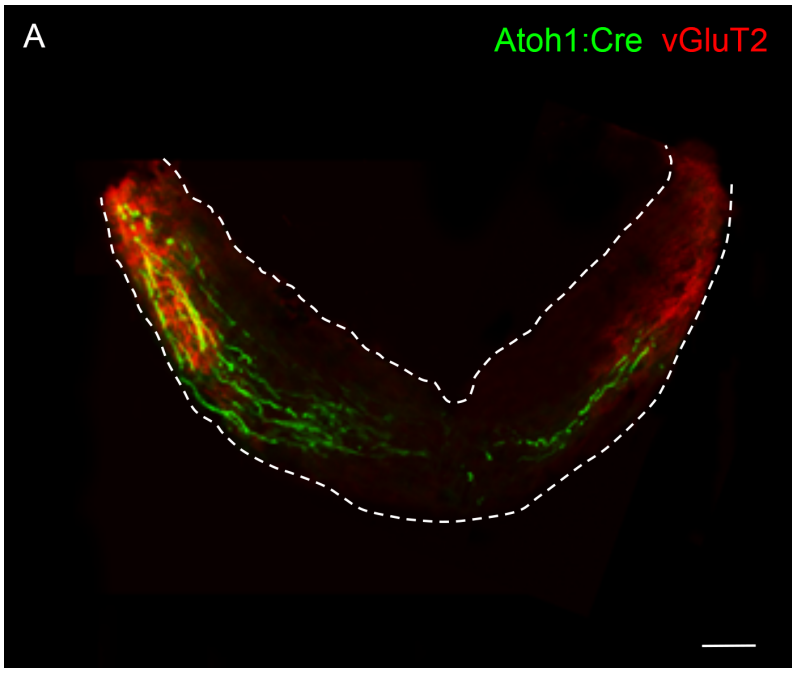

Figure S5. vGluT2 distribution in the axon course of Atoh1:cre transfected NM precursors. Transverse section of E4.5 hindbrain (r5) that was electroporated at E2.5 with Atoh1:cre-cGFP plasmid and stained for the vesicular glutamate transporter 2(vGluT2) (n=7 embryos). Scale bars: 200 μm in A.

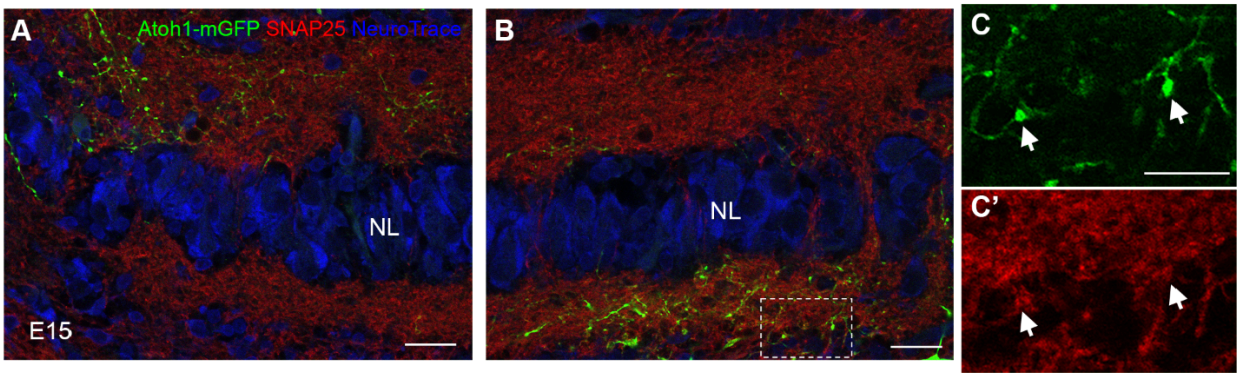

Figure S6. Atoh1-mGFP transfected axon terminals contain SNAP25. SNAP25 immunostaining was performed on the Atoh1-mGFP transfected E15 sections and counterstained with NeuroTrace. **A-B**: low magnification images of the ipsilateral (A) and contralateral (B) NL showing $mGFP^+$ axons in the dorsal and ventral NL neuropil regions, respectively. **C-C'**: High magnification images of the boxed area in B. $mGFP^+$ axon terminals (white arrows) are immunoreactive to SNAP25. Scale bars: 20 μm in A and B, 10 μm in C.

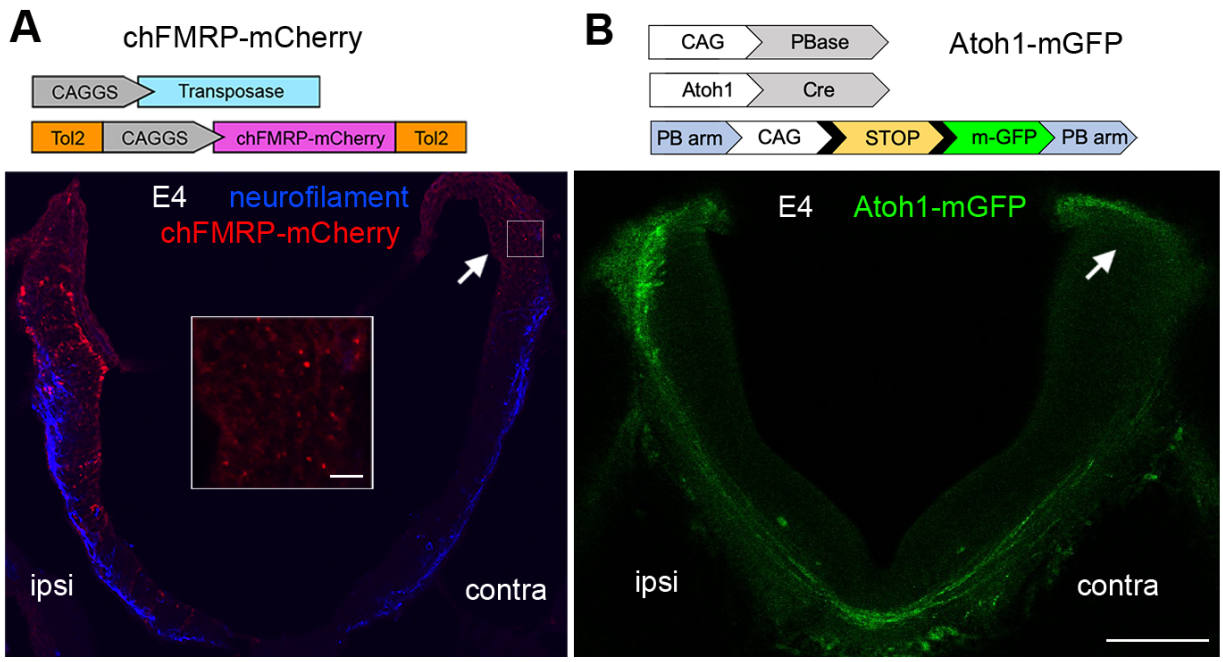

Figure S7. Axon localization of exogenous chicken FMRP (chFMRP) at E4. A. Transverse section from an E4 embryo electroporated with chFMRP-mCherry (red) at E2 and immunostained with neurofilament (blue), a marker for neuronal axons. mCherry^{+} puncta were detected in the dorsal hindbrain on the contralateral side (white arrow), where the axons of NM precursors terminate (see B). Inset shows an enlarged image of the boxed area. **B.** Transverse section from an E4 embryo electroporated with Atoh1-mGFP at E2 (green). mGFP^{+} axons extend contralaterally to the dorsal hindbrain, showing the approximate location of the auditory analogy (white arrow). Scale bars: 100 μm.

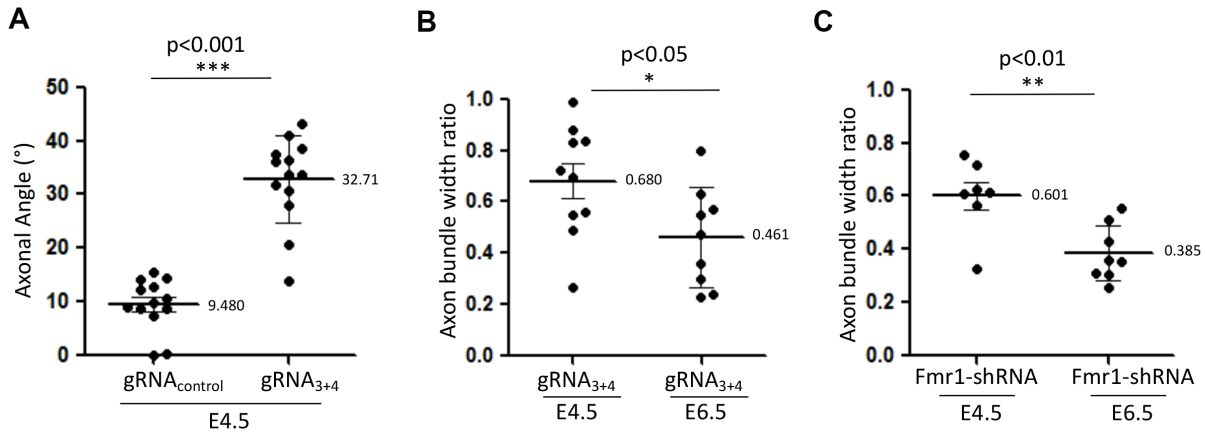

Figure S8. Additional data analyses in the Crispr-mediated FMRP knockout/knockdown studies. A, Crispr-mediated FMRP knockout alters the angle of projecting axons. Box plot analysis of the angle measured between a projecting axon and the mantle zone plane from E4.5 embryos electroporated with $gRNA_{control}$ (n=7) or $gRNA_{3+4}$ using ImageJ software. Each data point represents a mean angle value of 8 projections. Measurements included 13 sections for each treatment from 5 different embryos. **B,** Box plot analysis of the width of the GFP^+ axonal bundle measured in the circumferential axis in $gRNA_{3+4}$ electroporated embryos in E4.5 and E6.5. Each data point represents one embryo (n=10 at E4.5, n=9 at E6.5). The width of the axonal bundle is reduced at E6.5 in comparison to E4.5. **C**, Box plot analysis of the width of the GFP^+ axonal bundle measured in the circumferential axis in Fmr1 shRNA electroporated embryos in E4.5 and E6.5. Each data point represents one embryo (n=7 at E4.5, n=8 at E6.5). The width of the axonal bundle is reduced at E6.5 in comparison to E4.5. For each plot, the mean value is indicated.

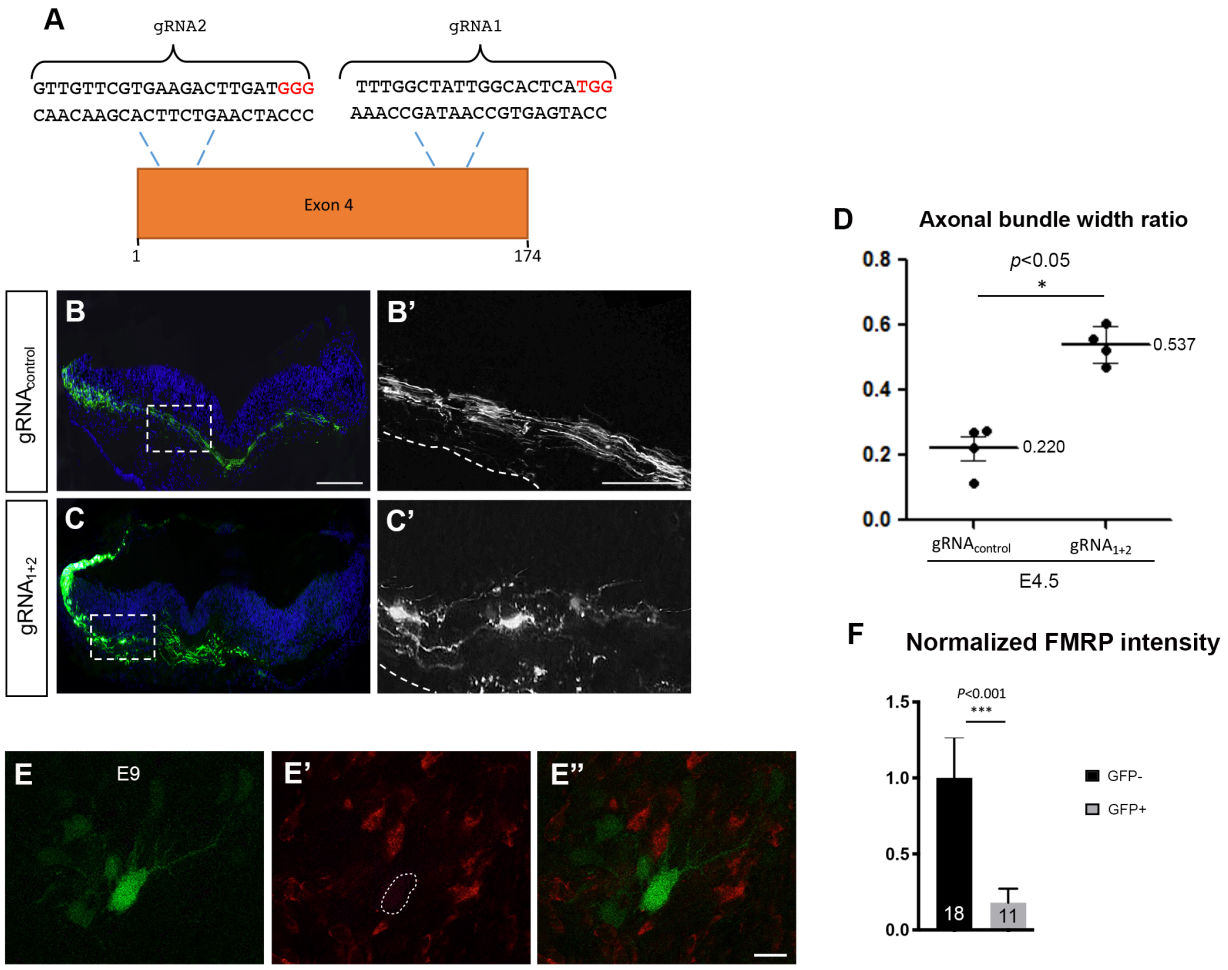

Figure S9. Crispr-mediated FMRP knockout induces axonal defasciculation. A. Crispr design of FMRP sequence in the region of exon 4. **B-C'.** Transverse sections of r5-6 level obtained from E4.5 embryos electroporated with $gRNA_{control}$ (B-B') or $gRNA_{1+2}$ (C-C') plasmids (n=4 embryos for each plasmid). Higher-magnification views of the boxed areas in the left panels (B,C) are represented in the right panels (B',C'). **D.** Box plot analysis of the width of the GFP^+ axonal bundle measured in the circumferential axis in $gRNA_{control}$ or $gRNA_{1+2}$ electroporated embryos. Each data point represents one section from one embryo. **E-E''.** Transverse sections from E9 embryos electroporated with $gRNA_{1+2}$ (green) and immunostained with FMRP antibody (red). The dashed circle surrounds to a transfected NM neuron that shows a loss of FMRP immunoreactivity as compared to neighboring non-transfected NM neurons. **F.** Bar graphs of normalized FMRP intensity, calculated as the corrected total cell fluorescence. Numbers on each bar indicate the number of neurons analyzed. Scale bars: 10 µm in B (applies to B and C), 50 µm in B' (applies to B' and C'), 10 µm in E'' (applies to E-E'').

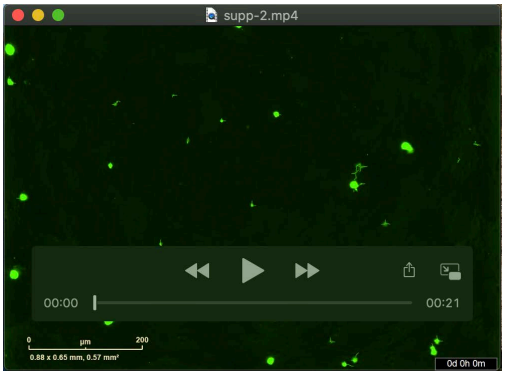

Movie 1

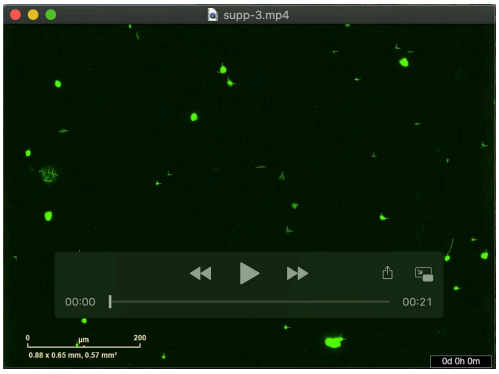

Movie 2

Movies 1 and 2. Time-lapse imaging of control and FMRP-knockout hindbrain cells in culture.

Time-lapse analysis of primary cell cultures prepared from entire hindbrains at E3.5. Hindbrains were electroporated at E2.5 with $gRNA_{control}$ plasmid (Movie S1) or $gRNA_{3+4}$ plasmid (Movie S2) to target the dA1 neuronal cell type. Cultures contained a mixture of electroporated (GFP^+) and non-electroporated cells. Cells were seeded in 48-well plates (n=6 wells for each treatment) and recorded every 6 hours for ~5 days. Time is indicated at the bottom right of the videos. In both movies, GFP^+ cells are clearly shown to extend neurites with time. Yet the neurite branching and extension rate is enhanced in Movie S2 compared to Movie S1. The corresponding still images from the time lapse imaging are presented in Fig. 9 of the main article.

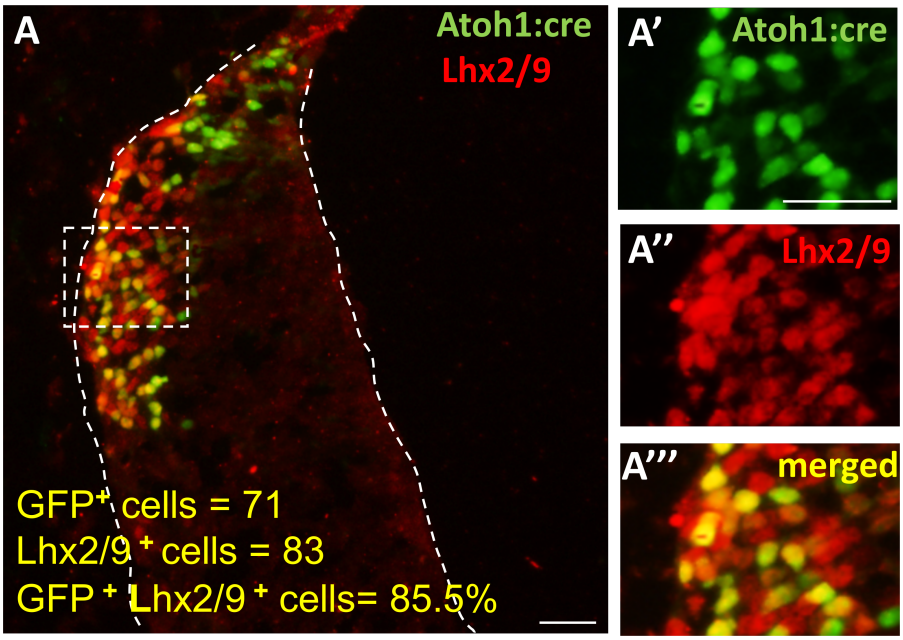

Figure S1. Atoh1:cre transfected cells are immunoreactive to Lhx2/9. Transverse section of E3.5 hindbrain (r5) that was electroplated at E2.5 with Atoh1:cre-nGFP plasmid and stained for Lhx2/9 to label endogenous dA1 cells. The dorsal half of the electroporated side of the neural tube is shown, demonstrating GFP^+ nuclei co-labeled with Lhx2/9 (n=7 embryos). Counting of cell nuclei expressing Atoh1:cre-GFP, Lhx2/9 or both in this section is provided in the lower left, demonstrating that 85.5% of electroporated cells co-express Lhx2/9. This ratio is in accordance with our previous publication (Kohl et al., 2012) that found 88% overlapping of Atoh1:cre with Lhx2/9 expressing cells. High-magnification views of the boxed area in (A) are represented in panels (A'-A''') in the different channels. Scale bars: 100um in A; 50um in A'.

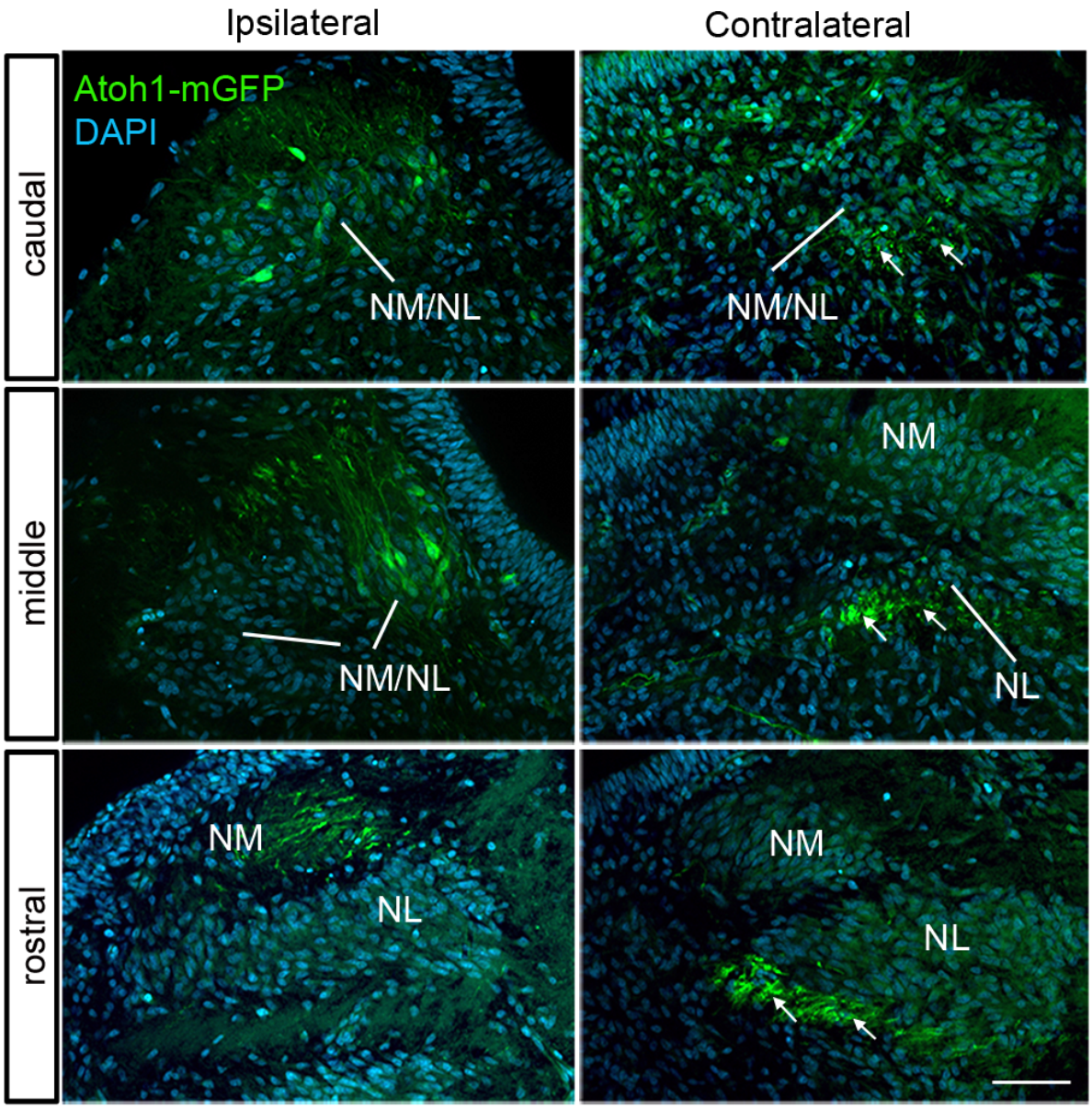

Figure S2. Separation of NM and NL at E7. Atoh1-mGFP labeling (green) at E7 on sections counterstained with DAPI (blue). At this stage, the NL and NM are migrating away from each other at the rostral level, while still merged at more caudal levels. White arrows point to the contralateral mGFP^{+} axons ventral to the NM/NL. Scale bars: 50 μm.

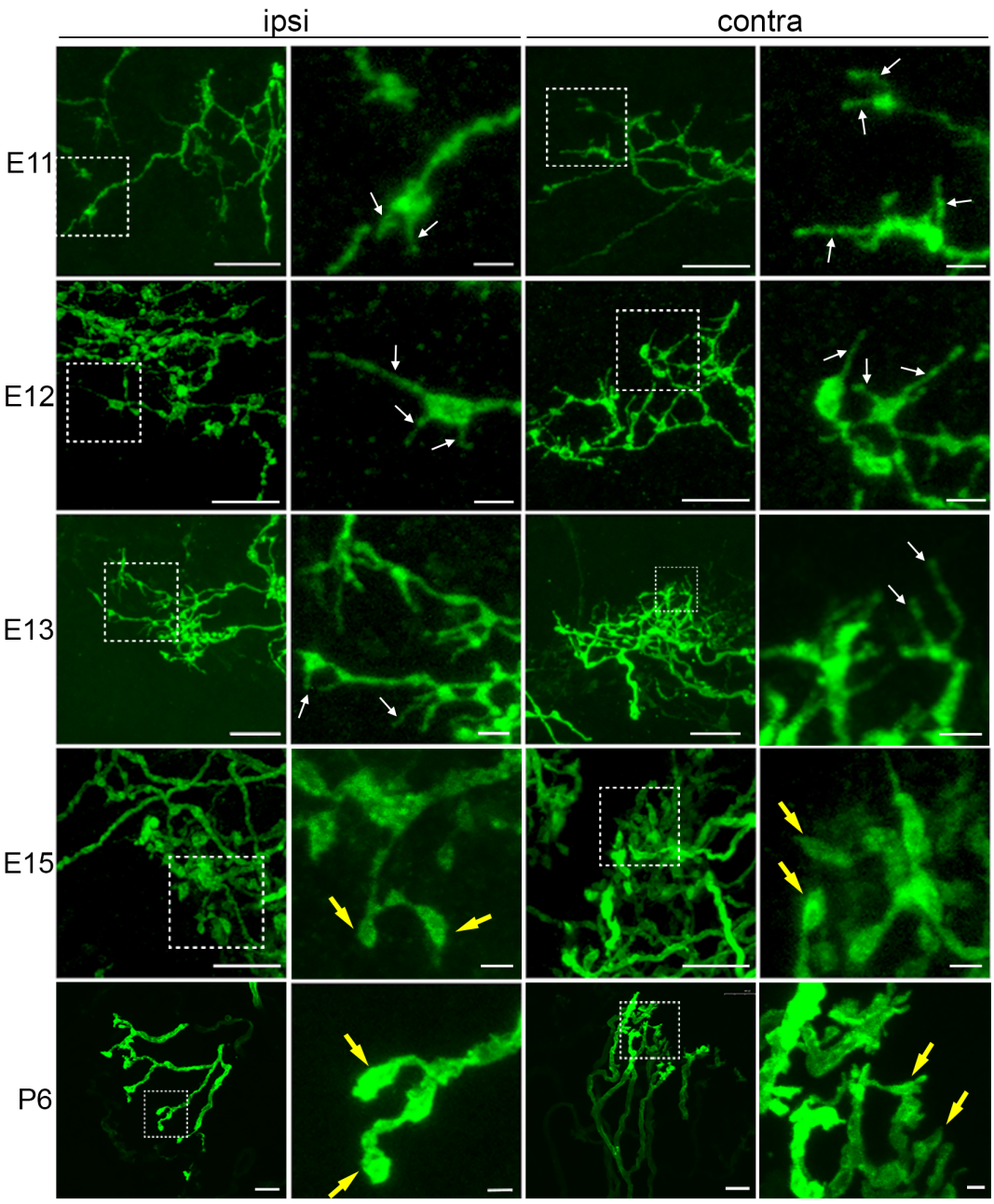

Figure S3. Morphological maturation of presynaptic terminals of NM neurons. Images were taken from embryos electroporated with Atoh1-mGFP at E2. The left two columns show NM axon terminals in the dorsal neuropil of the ipsilateral NL, while the right two columns show axons in the ventral neuropil of the contralateral NL. High-magnification views of the boxed areas appear in the right panel of each image. NM axons show a growth cone structure with filopodia (white arrows) at E11-13 and mature terminal morphology (yellow arrows) at E15 and later. Abbreviations: E, embryonic; P, post-hatch. Scale bars: 10 μm in lower-magnification images (columns 1, 3); 2 μm in higher-magnification images (columns 2, 4).

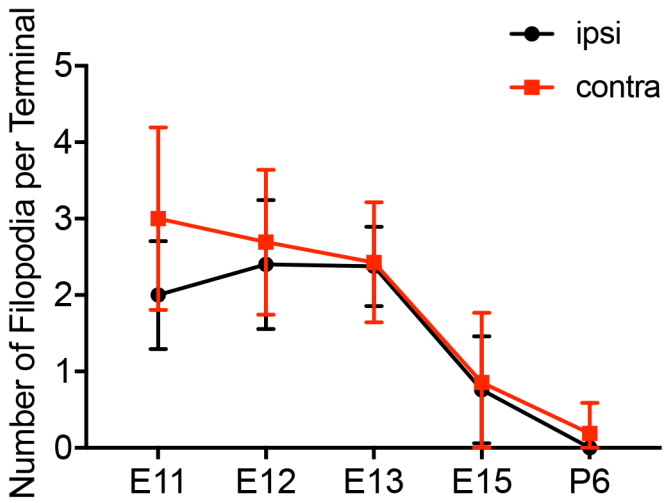

Figure S4. Quantification of terminal morphology at E11, E12, E13, E15 and P6.

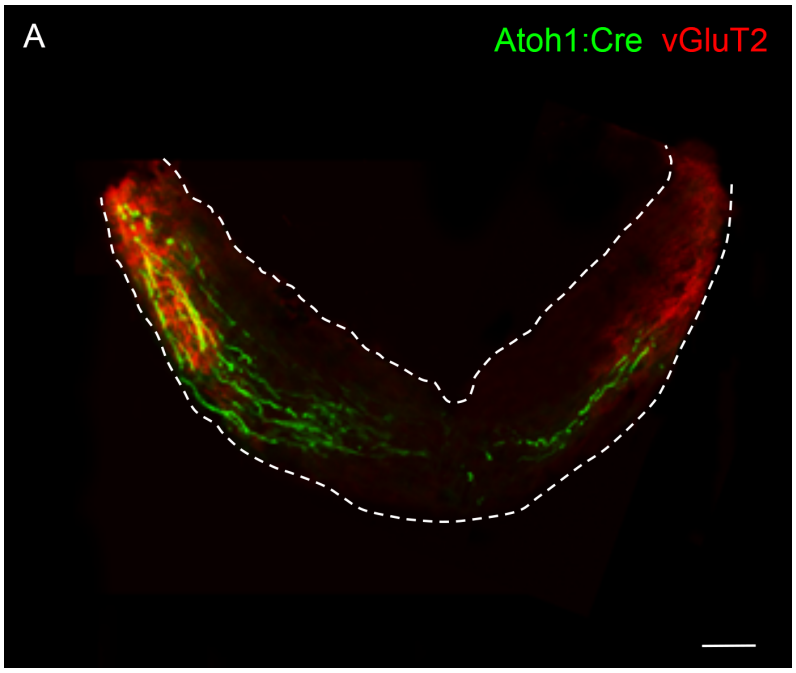

Figure S5. vGluT2 distribution in the axon course of Atoh1:cre transfected NM precursors. Transverse section of E4.5 hindbrain (r5) that was electroporated at E2.5 with Atoh1:cre-cGFP plasmid and stained for the vesicular glutamate transporter 2(vGluT2) (n=7 embryos). Scale bars: 200 μm in A.

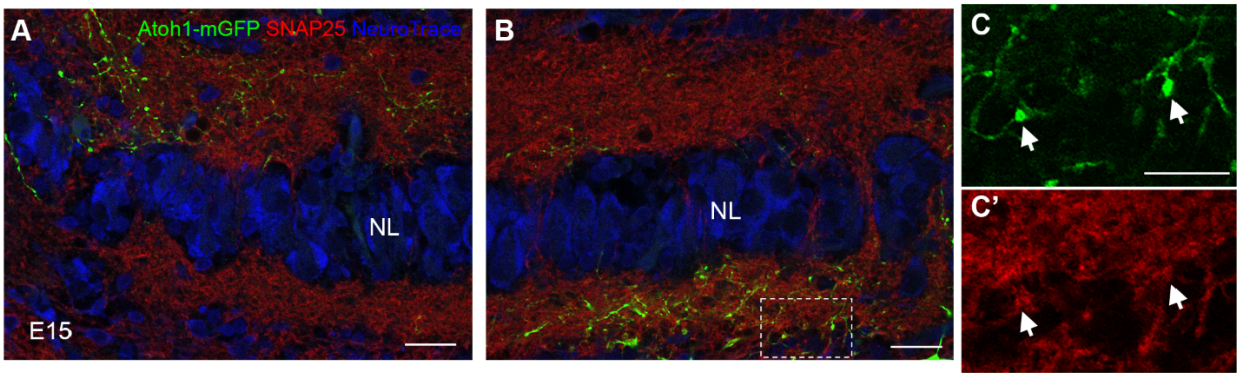

Figure S6. Atoh1-mGFP transfected axon terminals contain SNAP25. SNAP25 immunostaining was performed on the Atoh1-mGFP transfected E15 sections and counterstained with NeuroTrace. **A-B**: low magnification images of the ipsilateral (A) and contralateral (B) NL showing $mGFP^+$ axons in the dorsal and ventral NL neuropil regions, respectively. **C-C'**: High magnification images of the boxed area in B. $mGFP^+$ axon terminals (white arrows) are immunoreactive to SNAP25. Scale bars: 20 μm in A and B, 10 μm in C.

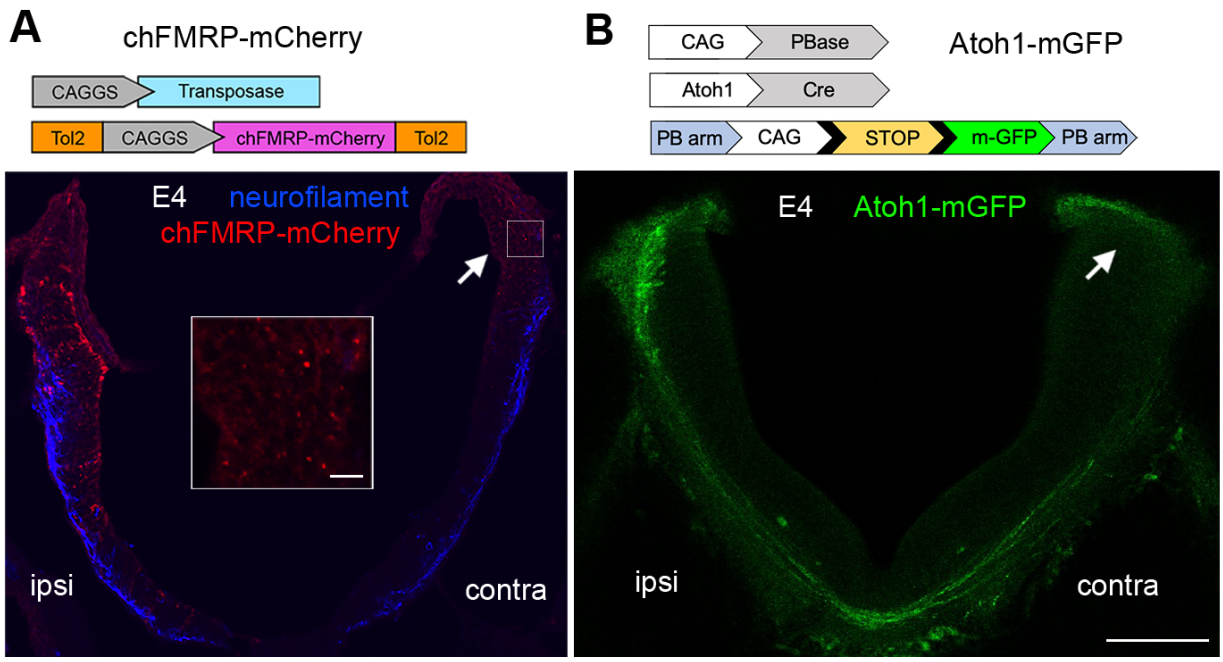

Figure S7. Axon localization of exogenous chicken FMRP (chFMRP) at E4. A. Transverse section from an E4 embryo electroporated with chFMRP-mCherry (red) at E2 and immunostained with neurofilament (blue), a marker for neuronal axons. mCherry^{+} puncta were detected in the dorsal hindbrain on the contralateral side (white arrow), where the axons of NM precursors terminate (see B). Inset shows an enlarged image of the boxed area. **B.** Transverse section from an E4 embryo electroporated with Atoh1-mGFP at E2 (green). mGFP^{+} axons extend contralaterally to the dorsal hindbrain, showing the approximate location of the auditory analogy (white arrow). Scale bars: 100 μm.

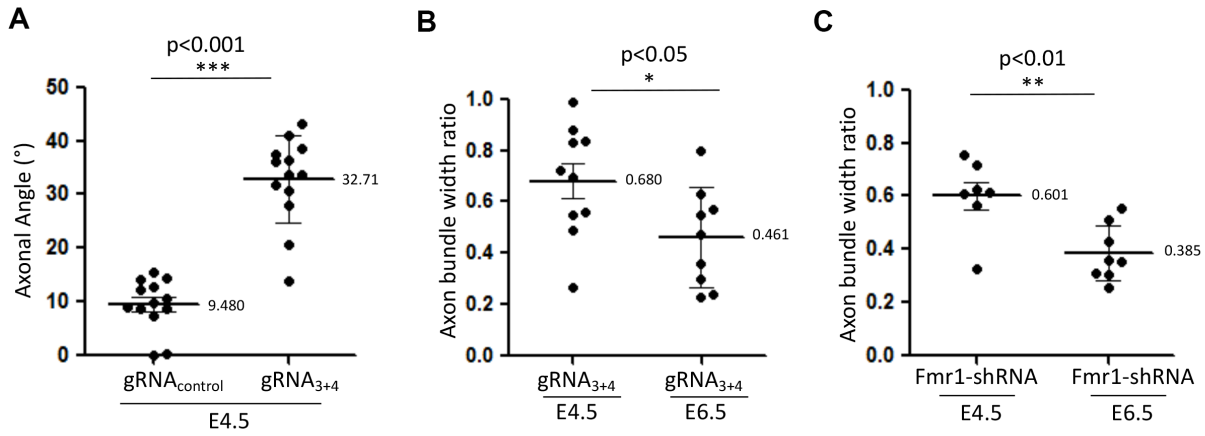

Figure S8. Additional data analyses in the Crispr-mediated FMRP knockout/knockdown studies. A, Crispr-mediated FMRP knockout alters the angle of projecting axons. Box plot analysis of the angle measured between a projecting axon and the mantle zone plane from E4.5 embryos electroporated with $gRNA_{control}$ (n=7) or $gRNA_{3+4}$ using ImageJ software. Each data point represents a mean angle value of 8 projections. Measurements included 13 sections for each treatment from 5 different embryos. **B,** Box plot analysis of the width of the GFP^+ axonal bundle measured in the circumferential axis in $gRNA_{3+4}$ electroporated embryos in E4.5 and E6.5. Each data point represents one embryo (n=10 at E4.5, n=9 at E6.5). The width of the axonal bundle is reduced at E6.5 in comparison to E4.5. **C**, Box plot analysis of the width of the GFP^+ axonal bundle measured in the circumferential axis in Fmr1 shRNA electroporated embryos in E4.5 and E6.5. Each data point represents one embryo (n=7 at E4.5, n=8 at E6.5). The width of the axonal bundle is reduced at E6.5 in comparison to E4.5. For each plot, the mean value is indicated.

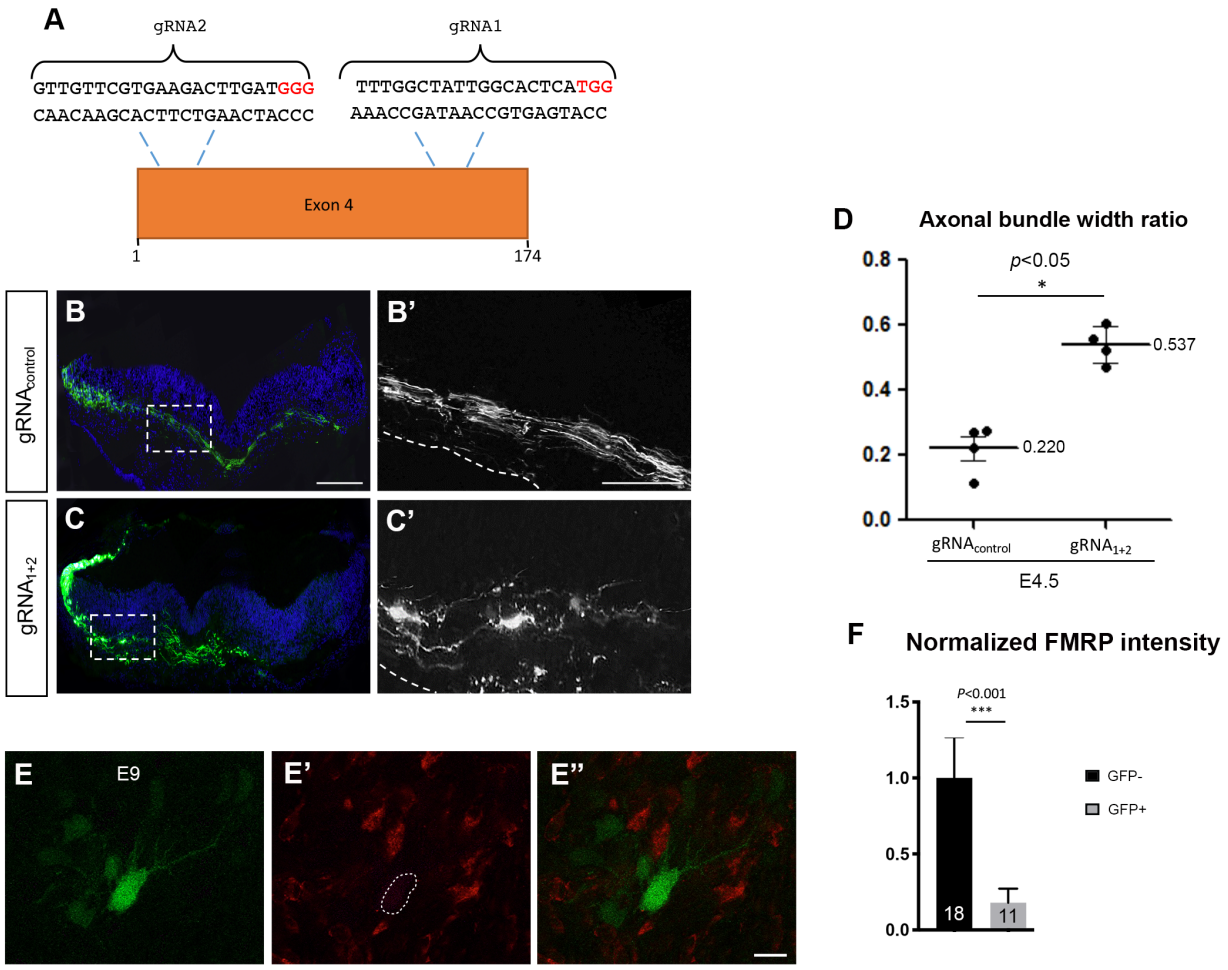

Figure S9. Crispr-mediated FMRP knockout induces axonal defasciculation. A. Crispr design of FMRP sequence in the region of exon 4. **B-C'.** Transverse sections of r5-6 level obtained from E4.5 embryos electroporated with $gRNA_{control}$ (B-B') or $gRNA_{1+2}$ (C-C') plasmids (n=4 embryos for each plasmid). Higher-magnification views of the boxed areas in the left panels (B,C) are represented in the right panels (B',C'). **D.** Box plot analysis of the width of the GFP^+ axonal bundle measured in the circumferential axis in $gRNA_{control}$ or $gRNA_{1+2}$ electroporated embryos. Each data point represents one section from one embryo. **E-E''.** Transverse sections from E9 embryos electroporated with $gRNA_{1+2}$ (green) and immunostained with FMRP antibody (red). The dashed circle surrounds to a transfected NM neuron that shows a loss of FMRP immunoreactivity as compared to neighboring non-transfected NM neurons. **F.** Bar graphs of normalized FMRP intensity, calculated as the corrected total cell fluorescence. Numbers on each bar indicate the number of neurons analyzed. Scale bars: 10 µm in B (applies to B and C), 50 µm in B' (applies to B' and C'), 10 µm in E'' (applies to E-E'').

Table S1. Plasmid sequences for gRNA production and validation.

	Exon of *Fmr1*	
G3	Exon8	GAGGTGGACCAACTACGTT
G4	Exon8	ACGTGGTCCAGGCTACGCTT
control		GGGTCTTCGAGAAGACCTG
Test-F3	Exon8	AGGTTGCTACCAGCTGTTGG
Test-F4	Exon8	TACTGCTATGAATAGCTCCTG
Test-R1	Exon8	GAAGCTATGTGCAAATATTAGCAG
Test-R2	Exon8	TTCTCATTGAACACTTGCATTTCC

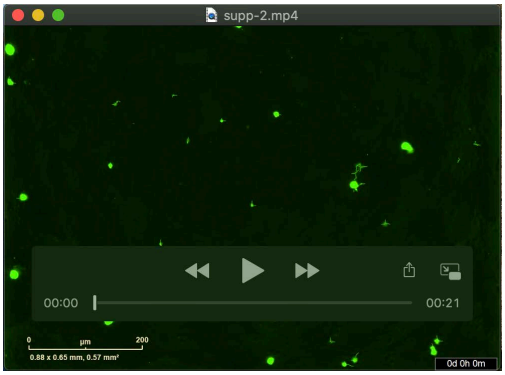

Movie 1. Control cells

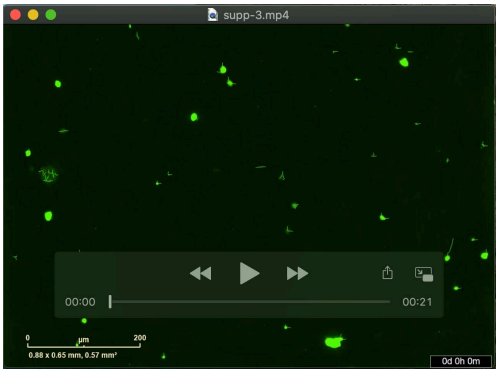

Movie 2. Manipulated cells

Movies 1 and 2. Time-lapse imaging of control and FMRP-knockout hindbrain cells in culture.

Time-lapse analysis of primary cell cultures prepared from entire hindbrains at E3.5. Hindbrains were electroporated at E2.5 with $gRNA_{control}$ plasmid (Movie 1) or $gRNA_{3+4}$ plasmid (Movie 2) to target the dA1 neuronal cell type. Cultures contained a mixture of electroporated (GFP^+) and non-electroporated cells. Cells were seeded in 48-well plates (n=6 wells for each treatment) and recorded every 6 hours for ~5 days. Time is indicated at the bottom right of the videos. In both movies, GFP^+ cells are clearly shown to extend neurites with time. Yet the neurite branching and extension rate is enhanced in Movie 2 compared to Movie 1. The corresponding still images from the time lapse imaging are presented in Fig. 9 of the main article.